Alginate-based copolymers as the solid-state electrolyte for Mg battery

Haozhe Liu

TU Delft

Alginate-based copolymers as the solid-state electrolyte for Mg battery

By

Haozhe Liu

in partial fulfilment of the requirements for the degree of

Master of Science
in Materials Science and Engineering

at the Delft University of Technology,
to be defended publicly on Thursday August 31, 2023 at 10:00 AM.

Student number: 5458323

Supervisor:	Dr. X. Wang	
Daily supervisor:	H. Wang	
Thesis committee:	Dr. X. Wang	TU Delft, RID
	Dr. Y. Gonzalez Garcia	TU Delft, MSE
	Dr. E.M. Kelder	TU Delft, RID

TU Delft

Abstract

The high theoretical volumetric capacity, abundance of magnesium in the earth's crust, and the relatively good safety features of Mg metal, have drawn great attention to developing Magnesium batteries as a follow-up to the success of Li-ion battery technology. However, the magnesium metal is incompatible with most electrolyte solvents and salts, which passivates the surface of magnesium and causes the battery failure. One of the crucial approaches to address this problem is to seek novel electrolytes which have good metallic Mg compatibility and subsequently improve the cycling performance.

In this research, the feasibility of combing PEO, Mg-alginate and $MgCl_2$ to design a solid polymer electrolyte (SPE) for Mg-ion batteries has been assessed. The SPE membrane shows a conductivity of ~10^{-5} S·cm^{-1} at 60 °C and an increased value up to ~10^{-4} S·cm^{-1} at 80 °C and above. The XRD results have suggested there is no real interaction in between the two polymers which can cause reconstruction of the polymer structure. Moreover, this electrolyte material is highlighted with an excellent cycling stability of up to 150 hours. At last, a possible model which could explain the Arrhenius behavior of temperature-dependent ion conduction is proposed for this SPE material. Overall, this research demonstrates the potential application of Mg-alginate for Mg energy storage in terms of developing a polymer electrolyte, despite further modification in the future is needed.

Content

List of figures

List of tables

Nomenclature

Abbreviations	Definition
AC	Alternating current
CV	Cyclic voltammetry
DC	Direct current
DME	Dimethoxyethane
DSC	Differential scanning calorimetry
EIS	Electrochemical impedance spectroscopy
GCD	Galvanostatic charge and discharge
LIBs	Lithium-ion batteries
PEO	Poly(ethylene oxide)
R&D	Research and development
RMBs	Rechargeable magnesium batteries
RT	Room temperature
SEI	Solid electrolyte interface
SHE	Standard hydrogen electrode
SPE	Solid polymer electrolyte
THF	Tetrahydrofuran
VTF	Vogel-Tammann-Fulcher
XRD	X-ray diffraction

1 Introduction

This chapter starts with a brief introduction on the background and motivation of this particular research topic, followed by basic theories behind the research framework. The research scope is also stated at the end of this chapter, aiming to provide readers with an overview before diving into the full text.

1.1 General background

Extensive research on 'beyond Lithium' electrochemical energy storage devices based on alternative metal cations has opened up new avenues for renewable and sustainable energy sources. Although considered as the current leading technology for electrochemical energy storage and conversion after decades of in-depth study, Li-ion batteries (LIBs) are still faced with severe challenges including safety issues and abundance concerns. The intrinsic property of lithium to grow needle-like crystals with subsequent plating/stripping cycles, known as dendrites, can cause internal short circuit and fire hazards [1]. Moreover, the geographically uneven distribution of lithium, cobalt, nickel and their potential depletion are of another growing concern regarding the large-scale manufacture of Li-ion battery industry. Thus, this motivates the exploration towards alternative resource-rich metal ion batteries without a trade-off on electrochemical performance, such as single valent Na^{+}, K^{+}, or multivalent Ca^{2+}, Zn^{2+}, Mg^{2+}, Al^{3+} [2]. Amongst these various candidates, Magnesium (Mg) based batteries have attracted significant attention, due to their high volumetric energy density, low safety concern, two-electron redox, as well as the large abundance and environmental friendliness of magnesium element [3].

Magnesium metal is an ideal anode material for both primary and secondary Mg-ion batteries thanks to a series of well-balanced properties. As shown in Fig. 1-1 (a), Mg possesses a low reduction potential of -2.37 V (versus standard hydrogen electrode (SHE)), which renders a relatively weaker reactivity than the active Li metal. It may also provide a possibility for battery cost reductions due to its natural abundance in the earth crust and seawater (8th and 3rd most abundant element respectively). More importantly, Mg exhibits a higher volumetric specific capacity than that for lithium metal (3,833 mA h cm^{-3} versus 2,046 mA h cm^{-3}) owing to the bivalent nature and small ionic radius (0.72Å) of Mg^{2+} [4]. Besides, unlike its Li counterpart, Mg metal anode does not develop dendritic but hemispheric or cauliflower-like deposition morphologies upon cycling, which are less prone to penetrate the separators and exempt Mg batteries from safety concerns [5]. However, implementing Mg anode practically is hindered by its strong tendency to form stable passivation surface films on contact with the majority of common solvents, which can completely block any electrochemical reaction from taking place. Details will be addressed in the next section.

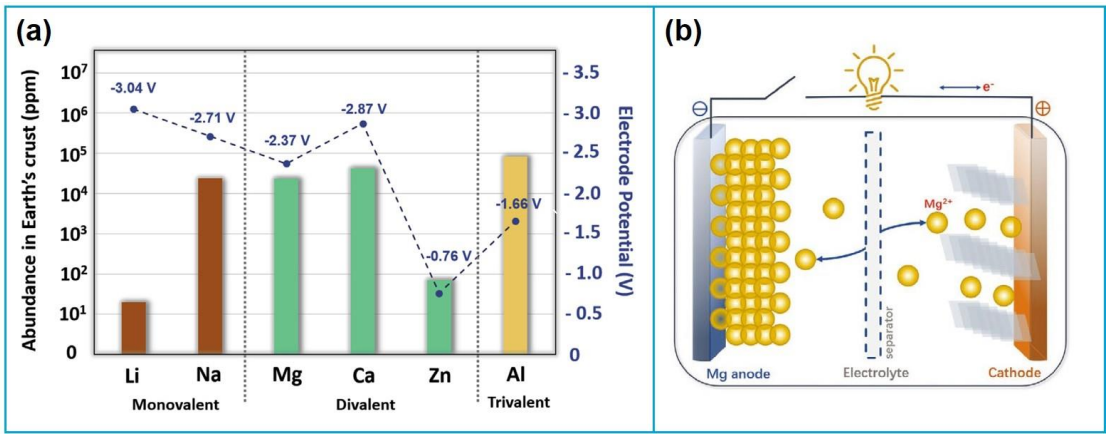

Fig. 1-1 (a) Schematic illustrating the abundance in earth's crust (bar chart, left y-axis), and electrode potentials (line chart, right y-axis) of elements that are of interest to the rechargeable metal-ion battery industry [6]. (b) Schematic of the working principle of secondary Mg-ion batteries [7].

1.2 Rechargeable Mg-ion batteries and challenges

Secondary Mg-ion batteries, also known as electrochemically rechargeable Mg batteries (RMBs) typically involve the reversible insertion and removal of Mg^{2+} in cathodes and anodes during charging and discharging, as depicted in the schematic (Fig. 1-1 (b)). It consists of an anode (in most cases Mg metal), a cathode, an electrolyte in between and a separator which isolates the two electrodes to avoid short circuit. The electrolyte is well recognized for its crucial role in the battery composition as the medium for ion transport between the two electrodes and charge transfer at the electrolyte/electrode interface. It is especially of greater importance in terms of the realization of RMBs in both laboratory and upcoming market. Unfortunately, since the first prototype of RMBs was successfully demonstrated in 2000 by Aurbach et al. with a combination of Mo_6S_8 cathode and Mg organo-haloaluminate electrolyte, the advancement of RMBs is still stuck in the lack of proper electrolytes and cathode materials despite after two decades of R&D [8].

Due to the low redox potential, Mg metal is highly reactive with reducible species in electrolytes, such as water and O_2 molecules. It is also incompatible with most polar aprotic solvents including carbonates and nitriles. The interfacial reaction can produce electron and ion insulating layers possibly composed of MgO and $Mg(OH)_2$, resulting in sluggish even no Mg^{2+} transport, high interfacial impedance, and large stripping/plating overpotential, thus inhibiting further electrochemical reaction [3]. The formed passivation layer is totally different from the surface film formed on lithium metal anode when analogous electrolytes are employed, referred to as solid electrolyte interface (SEI), which comprises ionic Li compounds and could effectively conduct Li-ions under electric field, as depicted in Fig. 1-2.

The unfavorable high reactivity of metallic Mg poses serious challenges in developing electrolytes for Mg-ion batteries, which is not as simple as replicating the analogs of Li systems. Challenges are also found in search for suitable cathode materials which allow for rapid intercalation/deintercalation of Mg^{2+}, especially at room temperature, because of the strong

electrostatic attraction of high-charge-density Mg^{2+} with the host material. Similarly, this binding interaction also results in complex solvation structure and thus sluggish diffusion kinetics within the electrolyte. To date, the systems that enable reversible Mg dissolution/deposition are mainly limited within ether-based organic electrolytes [9]. They mostly employ ethereal solvents which will not be reduced by Mg metal, such as tetrahydrofuran (THF) or glyme (also known as dimethoxyethane, DME), combined with custom-made complex salts, because typical simple salts e.g., magnesium perchlorate ($Mg(ClO_4)_2$ and magnesium triflate ($Mg(OTf)_2$) are not soluble and hard to disassociate in such solvents [10]. However, unfortunately, the ether-based solvents are readily volatile and flammable which are incompatible with the current policies of the European Union and impractical for real-world implementation. Accordingly, various types of novel electrolyte designs that are ether-free have been proposed over the years, with solid polymer electrolytes being one class of them.

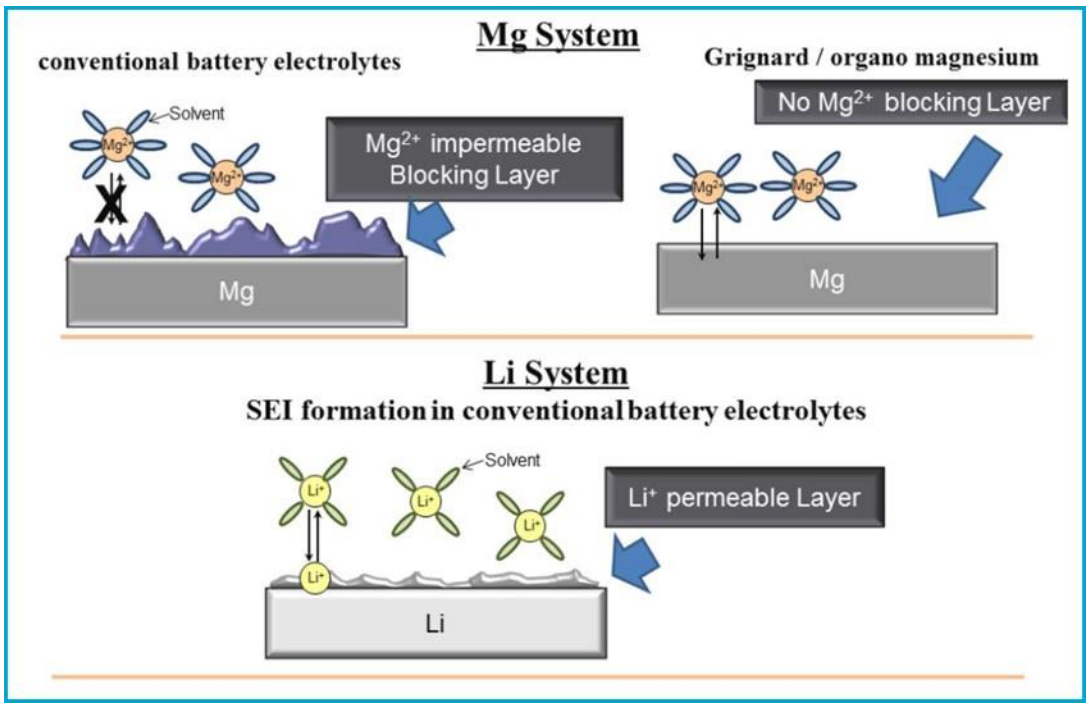

Fig. 1-2 Schematic depicting the simplified electrode–electrolyte interfaces for magnesium and lithium metals. The magnesium metal case unlike the lithium, forms a blocking layer when exposed to conventional electrolytes. In contrast, no Mg passivation occurs in ethereal organo-magnesium electrolytes [11].

1.3 Solid polymer electrolytes

Solid polymer electrolytes (SPEs) have the potential to replace the conventional organic liquid electrolytes especially for Mg-ion batteries due to improved properties in terms of overcoming the issue of interfacial passivation of Mg metal, and avoiding the risk of leakage and fire hazards. They tend to exhibit light weight, better shape flexibility and thus interfacial stability. SPEs, as one subgroup of solid-state electrolytes, also inherit the advantage of additional increasement in energy density by eliminating electrochemically inert separators in battery design. Featured

with well-recognized easy processibility, they are typically obtained by a straightforward synthesis procedure, involving dissolving the polymer host matrix, magnesium salt, and additives in solvents and subsequently being cast into thin films after removal of the solvent. Common polymer hosts include poly(ethylene oxide) (PEO), poly(ethylene glycol) (PEG), poly(vinyl alcohol) (PVA), poly(acrylonitrile) (PAN), polyvinyl pyrrolidone (PVP), poly(vinylidene fluoride) (PVDF), etc., among which PEO-based SPE is naturally the most studied one thanks to its verified success in Li-ion batteries [12]. The ionic conductivity and transference number of SPE depend on the dissociation ability of the salt in the polymer matrix and the chain segment motion of polymers [13]. To further improve the conductivity, researchers have also attempted to blend hybrid polymers to form a copolymer framework with cross-linked structure to suppress the polymer crystallinity. The polymer blends often exhibit properties that surpass the performance of each individual component polymer. So far, a result of 10^{-4} S cm^{-1} can be considered high for an SPE, even at somewhat elevated temperatures), as seen from Table 1-1. The research focus in this field is also still confined in optimizing the conductivity with limited evidence available about cyclability in Mg full cells. In addition to a high ionic conductivity which is the main function to shuttle ions of electrolytes, SPEs for Mg-ion batteries should also be required to have the following necessary properties: (1) No passivation films and corrosion with respect to Mg anode; (2) good chemical and electrochemical stability against the Mg metal anode; (3) High reversibility i.e., the ability to enable high Coulombic efficiency Mg electroplating and stripping; (4) other common properties essential for electrolytes, including low cost, non-toxic, non-flammable, etc. [14].

Table 1-1 Summary of ionic conductivity of reported magnesium-conducting SPEs. RT = room temperature. Reproduced from [12].

Mg salt	Polymer host	Filler	Ionic conductivity (S cm^{-1} at RT)
$MgCl_2$	PEO	-	$\sim 10^{-9}$
$Mg(TFSI)_2$	PEO	-	$\sim 10^{-7}$
$Mg(NO_3)_2$	PEO	-	1.34×10^{-5}
$Mg(NO_3)_2$	PEO-PVP	-	5.8×10^{-4}
$Mg(Tf)_2$	PEO-PPz	-	7.38×10^{-6} (50 °C)
$Mg(Tf)_2$	PEO	TiO_2, MgO	1.6×10^{-5}
$Mg(ClO_4)_2$	PEO	Al_2O_3	1.42×10^{-6}
$Mg(ClO_4)_2$	PEO	MgO	2×10^{-6}
$Mg(CH_3COO)_2$	PEG	TiO_2	1.06×10^{-4} (30 °C)
$Mg(Tf)_2$	PVA	-	5.41×10^{-4}
$Mg(NO_3)_2$	PVA-PEG	-	9.63×10^{-5} (30 °C)
$Mg(NO_3)_2$	PVA	-	7.36×10^{-7} (30 °C)
$Mg(CH_3COO)_2$	PVA	-	1.34×10^{-7} (30 °C)

$Mg(ClO_4)_2$	PVA-PVP	-	1.1×10^{-4}
$Mg(ClO_4)_2$	PVA-PAN	-	2.96×10^{-4}
$Mg(NO_3)_2$	PVA-PAN	-	1.71×10^{-3}
$Mg(ClO_4)_2$	PEC	-	5.2×10^{-5} (90 °C)
$Mg(TFSI)_2$ + LiFSI	PEC	-	1.0×10^{-5} (80 °C)
$Mg(Tf)_2$	PVdF-HFP	-	$\sim 10^{-3}$
$Mg(ClO4)_2$	PVdF-HFP/PVAc	-	1.60×10^{-5} (30 °C)
$Mg(NO_3)_2$	PVdF	MgO	1.04×10^{-4}

1.4 Poly(ethylene oxide) structure and its conduction mechanism

Since the first report of ion conducting poly(ethylene oxide) (PEO)-based SPE in 1970s, PEO has developed as the major polymer host matrix used in various polymer electrolyte chemistries including Mg^{2+} conducting electrolytes [15]. PEO has the same linear structure of H-(O-CH_2-CH_2)$_n$-OH as polyethylene glycol (PEG) depending on its molecular weight (PEO typically has molecular weight above 20,000 g/mol). It is a semi-crystalline polymer with high degree crystallinity of 75% ~ 80% and the rest is amorphous rubbery phase at room temperature [16]. It also has a well below zero glass transition temperature (T_g) of -60 °C and a melting point (T_m) of about 65 °C. The low T_g ensures a good polymer segmental mobility desired for ion conduction at room temperature and above. In light of this, the polymer electrolytes are formed by dissolving low lattice energy salts in the PEO host matrix. The salts disassociate and then the cations can coordinate with the ether group (-O-) via liable bonds which means the metal-ligand bonds are easy to broken and ions can move to the next vacant site [17].

The ion conduction in PEO-based SPE is recognized to principally occur in the amorphous region. Although the conduction mechanism is not completely made clear, researchers have commonly accepted the assumption that cations can move along the polymer backbone in the amorphous part through coordination – release – re-coordination with the functional groups of polymer chain (ether oxygens for PEO) [18]. When subject to an electric field, the polar ether group can become polarized and form dipoles which can interact with the cations via electrostatic force. There are two different models which can explain different behaviors of the ion transport in SPE, namely the Arrhenius model and the Vogel-Tammann-Fulcher (VTF) model. The Arrhenius equation is described as follows, which can model long range ion transport as a consequence of cation hopping instead of the motion of polymer molecule:

$$\sigma(T) = \sigma_0 \exp\left(-\frac{E_a}{k_B T}\right) \qquad (1-1)$$

where σ_0 is the pre-exponential factor, E_a is the activation energy, k_B is the Boltzmann constant, T is the temperature. Another empirical model is called the VTF model which is in agreement

with the free volume theory, as described in Eq. 1-2:

$$\sigma(T) = AT^{-\frac{1}{2}} \exp\left(-\frac{B}{k_B(T - T_0)}\right) \qquad (1-2)$$

where A is a pre-factor, B is pseudo-activation energy associated with polymer segmental motion and $T_0 = T_g - 50k$. It can be used to model strong correlations of ion transport and polymetric segments movement. For PEO-based electrolytes, the ionic conductivity obeys the Arrhenius relationship under T_m at which the polymer segmental motion is mild due to large extent of crystalline phase present. The conductivity gradually increases with temperature because the ion mobility increases and dominates. This is similar to the case of inorganic solid ionic conductors. At temperature above T_m, the VTF behavior starts to play a role, as the ionic conductivity features a curve versus the inverse of temperature. This can be explained that high temperature leads to the expansion of free volume and thus promotes the segmental motion of ionic charge carriers i.e., the polymer chain segments. In fact, the improved ionic conductivity is a combined effect at high temperature, that is to say, the dynamic motion of the host polymer chain either carries cations to migrate, or facilitates ions to jump from one site to another intra-chain or inter-chain site [18]. Based on the above discussion, the typical curves for each mechanism are shown in Fig. 1-3.

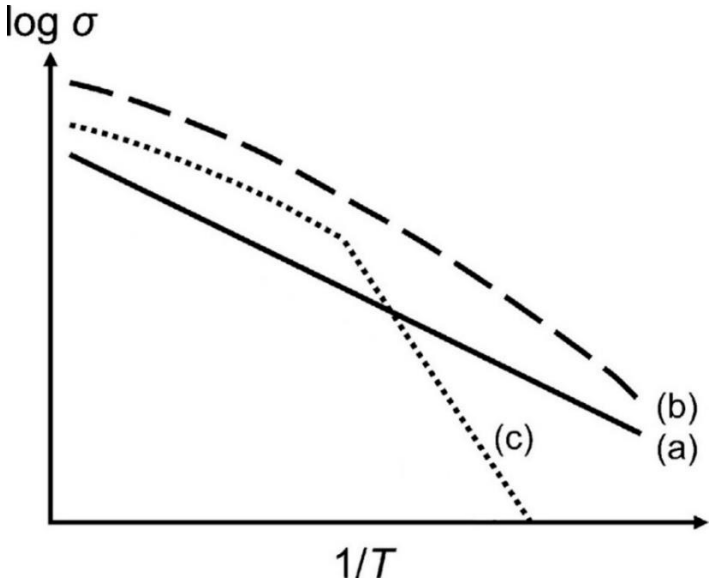

Fig. 1-3 Idealized ionic conductivity behaviors of SPE. (a) The linear Arrhenius behavior, typical for rigid polymer systems. (b) The curved VTF behavior for completely or highly amorphous SPE. (c) The behavior with two well-defined regions representative of semi-crystalline polymer which has a certain Tm within the temperature range, for example the PEO system [16].

1.5 Influence of solvent absorption and humidity on the performance of SPE

Water content significantly influences the conductivity of SPE, boosting even up to several orders of magnitude depending on the identity of salt as well as content of water and salt [19]. Due to the hydrophilic and hygroscopic nature of some salts that SPE may contain and ether

oxygens of PEO, water is inadvertently absorbed during atmospheric exposure. Small amount of water even at ppm-level can help decrease polymer crystallinity and increase mobility of ions [20]. As we know from the discussion on PEO ion conduction mechanism, these changes are beneficial to achieve a good conductivity. Therefore, it is difficult to decouple and identify real contributions from the alterations in materials optimization that we are interested in. Although it is relevant to realize a dry environment to assemble and test the materials completely in the glovebox, the experimental set-up is rather complex especially in the case that elevated temperature measurements are needed. So, the experiments are commonly conducted in a low humidity atmosphere.

1.6 Structure and possible ion conducting properties of magnesium alginate

Alginate is a class of polysaccharide typically extracted from brown seaweeds. It is environmentally benign, non-toxic and abundant in nature, which justifies the broad use in food, cosmetics, and biomedical industry due to its good biocompatibility and relatively low cost. Basically, alginate is a linear anionic copolymer which contains monomer blocks of (1,4)-linked α-L-guluronic acid (G) and β-D-mannuronic acid (M). These monomer residues are covalently linked in different orders and form three block types: consecutive G residues, consecutive M residues and alternating G and M residues, as shown in Fig. 1-4. Due to the rich presence of carboxyl ($-COO^-$) and hydroxyl (-OH) groups, it is well-known for its coordination properties, for example binding with divalent ions such as Ca^{2+} and Ba^{2+}. In this case, cations can interact with alginate chains via electrostatic attraction with negatively charged carboxyl groups, resulting in the formation of hydrogels with crosslinked network. Only the G blocks are believed to take effect owing to the buckling shape where exists cavity to capture the positively charged cations such as Ca^{2+}. This structure is termed the egg-box model, as illustrated in Fig. 1-5. The calcium ions are positioned inside the intermolecular interstices like eggs caged in a cardboard box. However, unlike the strong complexion between Ca^{2+} and alginate, Mg^{2+} has relatively lower affinity to alginate (the lowest in the series of multivalent cations) [21]. Donati et al. proposed that Mg^{2+} has a diffusively bound behavior and is still free to move, despite there is limited experimental evidence on this [22]. This is in essence beneficial for ion conduction in terms of using magnesium alginate to fabricate the electrolytes because magnesium ions are expected to hop along the polymer chain and Mg^{2+} inter-chain movement is also possible. Moreover, the gelation of alginate with Mg^{2+} is a slow process, which is in stark contrast to the Ca^{2+} induced instantaneous hydrogel formation [23]. It is also unstable and prone to dissolve. Generally, the physicochemical characteristics of resultant hydrogels all depend heavily on the M/G ratio of the raw material.

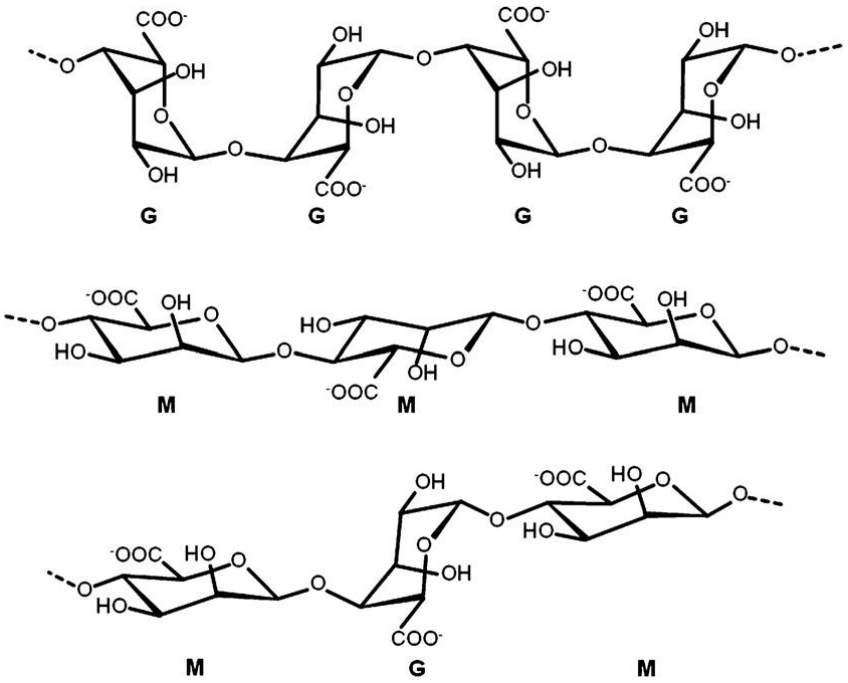

Fig. 1-4 The structures of G-block, M-block, and alternating G-M-block in alginate [24].

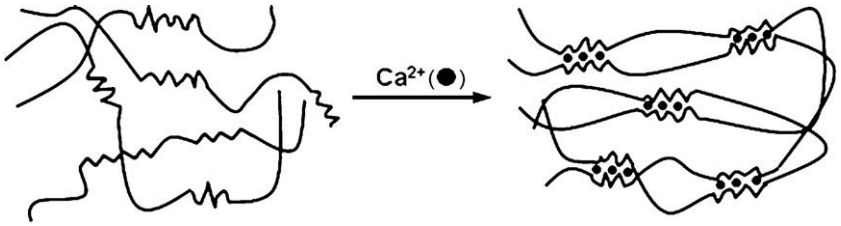

Fig. 1-5 Illustration of the egg-box model with interstices occupied by calcium ions [24].

1.7 Scope of this master thesis project

Based on the above discussions on the ion conduction properties of PEO and Mg-alginate, there emerges a high chance to combine them and design as a solid polymer electrolyte. The PEO provides a host matrix to compensate for the poor mechanical properties of the rigid and brittle alginate film. To the best of our knowledge, no study is available on this combination in the literature before, even no concrete experimental evidence on the use of Mg-alginate as electrolyte materials prior to this study. With the two polymers brought together, the research question then becomes:

Is PEO and Mg-alginate a good combination of copolymer electrolyte for Mg-ion batteries?

In this master thesis research, most attention will be paid to assessing the ionic conductivity of the copolymer system, since it is of fundamental importance when benchmarking an SPE material. Several composition parameters were adjusted and optimized to formulate the best conductivity. Galvanostatic cycling is performed via Mg symmetric cell to evaluate the cycling stability of this SPE. The physicochemical properties will also be accordingly analyzed to

account for the structural basis. Before diving into the thesis experimental framework, the characterization techniques are reviewed with the purpose to help readers better understand the data interpretation. At last, conclusions will be drawn in order to answer the research question.

2 Characterization techniques and data interpretation

This chapter intends to go over the fundamentals of each characterization technique covered throughout this research. The general theories are also addressed with specific focus towards application on solid polymer electrolyte study. The guidelines to interpret the obtained data will also be provided, hoping to assist readers and colleague researchers with a clear understanding on the physical meaning of data.

2.1 Electrochemical impedance spectroscopy

Electrochemical Impedance Spectroscopy (EIS) is an alternating current (AC) -based non-destructive electrochemical technique. EIS uses a small sinusoidal voltage E(t) (termed "Potentiostatic EIS", PEIS) or current I(t) ("Galvanostatic EIS", GEIS) to perturb an electrochemical system and measure the consequent response which reveals information about processes happening at different time scales. At high frequencies, only quick processes such as charge transfer are able to respond, while at low frequencies, mass transfer or diffusion dominates [25]. In the case of PEIS, the angular frequency (ω) dependent impedance Z(ω, t) is defined as the ratio of the sinusoidal alternating potential signal E(ω, t) to the current response of the same frequency I(ω, t), as expressed in Eq. 2-1, where E(ω, t) and I(ω, t) can be expanded in sinusoidal functions, and |ΔE|, |ΔI| is the peak voltage, current amplitude respectively, ϕ is the phase delay between E and I [26].

$$Z(\omega,t)=\frac{E(\omega,t)}{I(\omega,t)}=\frac{|\Delta E|sin(\omega t)}{|\Delta I|sin(\omega t+\phi)} \qquad (2-1)$$

Z could also be represented as a complex containing a real part and an imaginary part: Z_{Re} (ϕ = 0°) and Z_{im} (ϕ = 90°) by using Euler's formula, as shown in Eq. 2-2,

$$Z=|Z|e^{-i\phi}=Z_{Re}-iZ_{im} \qquad (2-2)$$

where |Z| is the modulus and equals $\sqrt{Z_{Re}^2+Z_{im}^2}$.

EIS is a powerful analysis tool in the field of solid-state batteries research. It is widely used to probe the physical and chemical processes occurring at the bulk and interfaces of various solid-state chemistries. Although interpreting the complex spectra is currently non-normalized and often challenging, researchers have reached a consensus that the ionic conductivity of solid electrolytes can be assessed using the equation below by two-ion-blocking-electrode measurement:

$$\sigma_{ion}=\frac{t}{R_{total}A} \qquad (2-3)$$

where R_{total} is the total resistance of the electrolyte sample extracted from the EIS spectra, A is the geometrical area and t is the thickness. Ion-blocking electrodes such as stainless steel (SS) or platinum (Pt) do not accept or provide any ion which means no Faradaic reactions taking place, but they can allow electron conduction.

The data of EIS measurement could be displayed in two different types of plots: the Nyquist plot (Imaginary Z component vs. Real Z component) and the Bode plot (The modulus or phase angle of Z vs. Frequency). Example spectra of a typical solid-state electrolyte are shown in Fig. 2-1. The Nyquist plot mainly presents a semi-circle on the real axis with a diameter of R_{ct}, which also has an offset R_s from the origin. The curve can be modelled with the proposed equivalent circuit depicted in Fig. 2-2 generated from the *ZView*® software. The series resistance R_s which may include the resistances of wires, the SS electrodes and the bulk electrolyte, is in series with the charge transfer resistance R_{ct} which is then in parallel with a constant phase element (CPE). The R_{ct} describes the resistance associated with the transfer of charge carriers at the electrode/electrolyte interface, specifically the SS/SPE interface in this case. The CPE is basically an imperfect capacitor that is used to simulate the non-ideal capacitive behavior of the electrical double layer at the SS/SPE interface, which may be caused by the inhomogeneity and unevenness of the material surfaces. The R_{ct} and CPE together account for the impedance contributions from the interface. Furthermore, the R_{total} in Eq. 2-3 can be referred to as $R_s + R_{ct}$. It is worth noting that equivalent circuits are black-box models which means multiple models may be equally efficient to fit one set of experimental data [27]. The choice of equivalent circuit models is highly empirical and subjective as long as they are able to match the data.

The Bode plot is usually used in complement to the Nyquist plot. It relates the impedance data with time domain, which indicates information about specific contributions of different components with respect to their time scale.

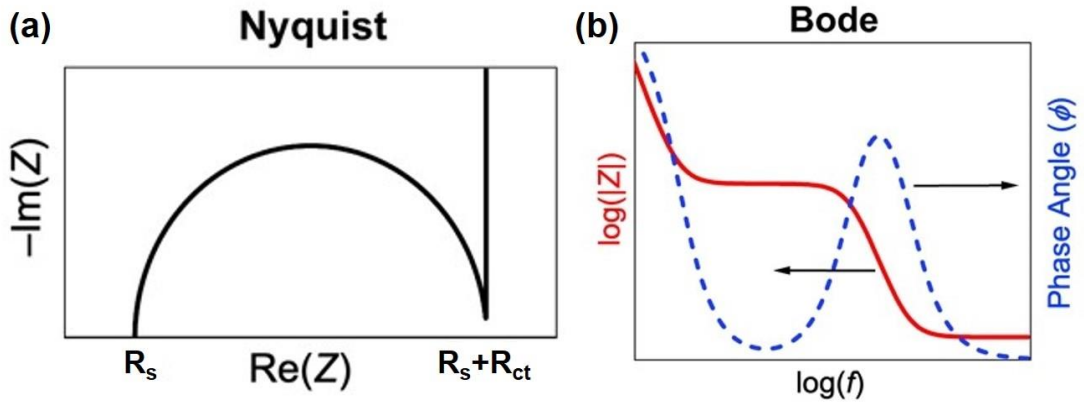

Fig. 2-1 Example spectra of a typical solid-state electrolyte (a). Nyquist plot. (b). Bode plot. Reproduced from [25]

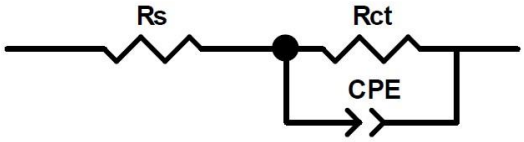

Fig. 2-2 A possible equivalent circuit for solid-state electrolytes.

2.2 X-ray Powder Diffraction

As a fast and non-destructive analytical technique, X-ray Powder Diffraction, as one common approach of X-ray Diffraction (XRD), is used to identify the chemical composition of unknown crystalline materials based on Bragg's law, described in the following Eq. 2-4:

$$n\lambda = 2d \sin\theta \qquad (2-4)$$

where n is an integer, λ is the wavelength of X-ray that is employed, d is interlayer spacing and θ is the angle between the incident X-ray and the crystal lattice planes. Experimentally, X-ray powder diffraction irradiates monochromatic X-ray beam on the sample with varied incident angles, in contrast to the Laue diffraction method where X-ray beam of continuous wavelength (broad spectrum) is used with the θ fixed [28]. The visualization schematic of Bragg diffraction is shown in Fig. 2-3. When Bragg's equation is satisfied, constructive interference will occur at a radiation path difference of nλ, leading to the presence of diffraction peaks in the final profile. The peak position provides information about the phase composition and lattice spacing by comparing to the standard reference pattern. From the peak shape, physical properties such as grain size, micro-strain and stress could also be derived. Besides, XRD is considered suitable to study semi-crystalline polymers such as PEO in this research. Sharp peaks can be found in the diffraction pattern when crystalline parts are detected while amorphous parts produce broad and diffuse peaks, as seen from Fig. 2-4. This can further help to determine the crystallinity of polymers.

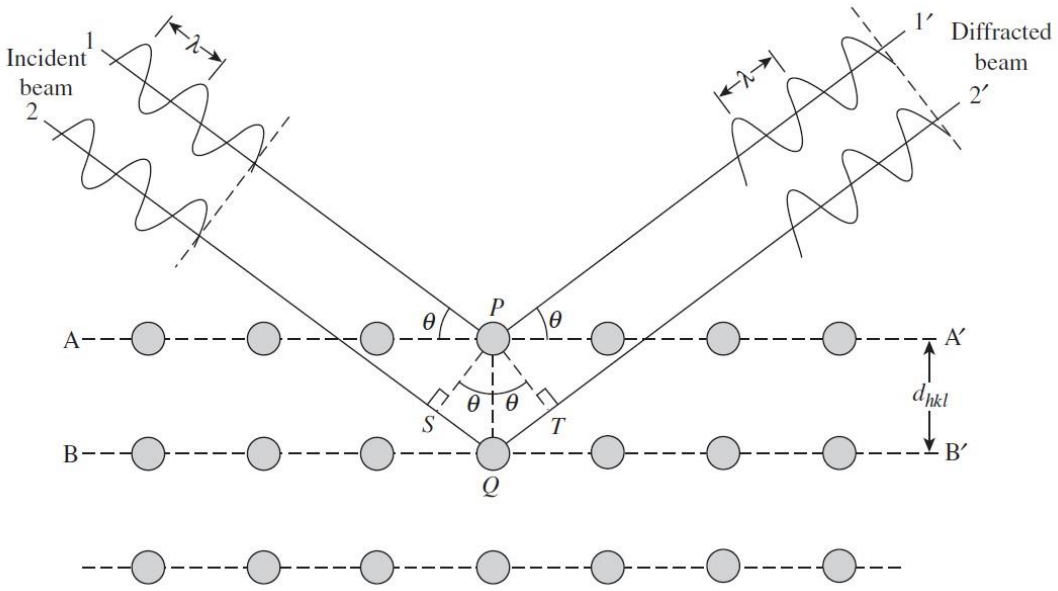

Fig. 2-3 Visualization of Bragg's law. The path difference between beam 1 and 2 is SQ + QT = 2 PQ sinθ [29].

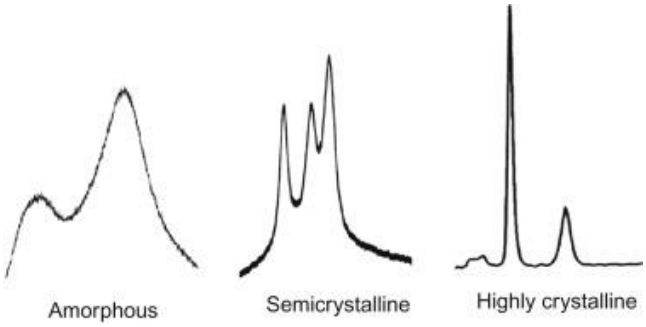

Fig. 2-4 Characteristic peaks for different polymer phases [28].

2.3 Differential scanning calorimetry

Differential scanning calorimetry (DSC) appears powerful in investigating the thermodynamic properties of materials, especially for polymers. It is designed to measure the difference between the heat flows into a sample and a reference as a function of temperature. There are two primary types of DSC systems: the power-compensated DSC and the heatflux DSC which is also selected for this research. In the heatflux DSC, the sample and the reference are kept inside the same linear-temperature-controlled furnace equipped with thermocouples to monitor the temperature. Due to their different heat capacities (C_p), there will be a difference in the real temperature of the sample and reference (ΔT), which leads to the heat flow between them based on the following equation:

$$q = \frac{-\Delta T}{R} \qquad (2-5)$$

where q is the heat flow, ΔT is the temperature difference and R is the thermal resistance [30]. On top of the heatflux DSC, there emerges an advanced system named temperature-modulated DSC in which the steadily linear heating rate is modulated by superimposing a sinusoidal signal. This effect is able to separate the reversing (e.g., glass transition, melting) and non-reversing (e.g., curing, relaxation) thermal events and provide in-depth details. In the power-compensated DSC, the sample and reference are separated in two different furnace chambers with individual heating systems. The sample and reference are maintained in the same temperature and the electrical power required for this equilibrium is recorded as a function of temperature or time.

Common thermal properties measured by DSC include glass transition temperature (T_g), melting temperature (T_m), crystallization, phase transformations, curing kinetics, etc. An example DSC curve is illustrated in Fig. 2-5 in which the heat flow is plotted versus temperature. Conventionally, the endothermic event which means the heat is transferred into the sample is plotted upwards against the baseline on the curve. However practically, one has to always refer to the actual arrow indication. As seen from the graph, the glass transition is a stepwise shift on the curve due to the change in heat capacity between the glassy state and the rubbery state of polymers, while the first order transition melting/crystallization shows as a peak. The onset temperature of a peak (T_{onset}) is often considered to be the temperature at which the phase transformation begins, for example the melting temperature (T_m) and the crystallization temperature (T_c). This is attributed to the fact that it is not prone to be influenced by the mass of the tested sample compared to the peak temperature (T_{peak}) which is associated with the

change in peak area. In practice T_{onset} is defined as the intersection of the slope at the inflection point on the peak and the slope of the baseline before the peak, as drawn in Fig. 2-6.

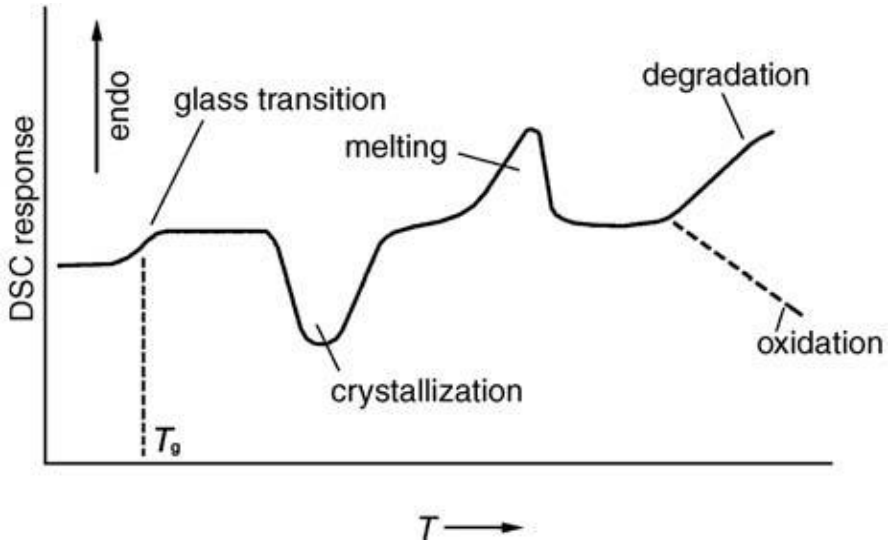

Fig. 2-5 Example of DSC curve for a polymeric sample [29].

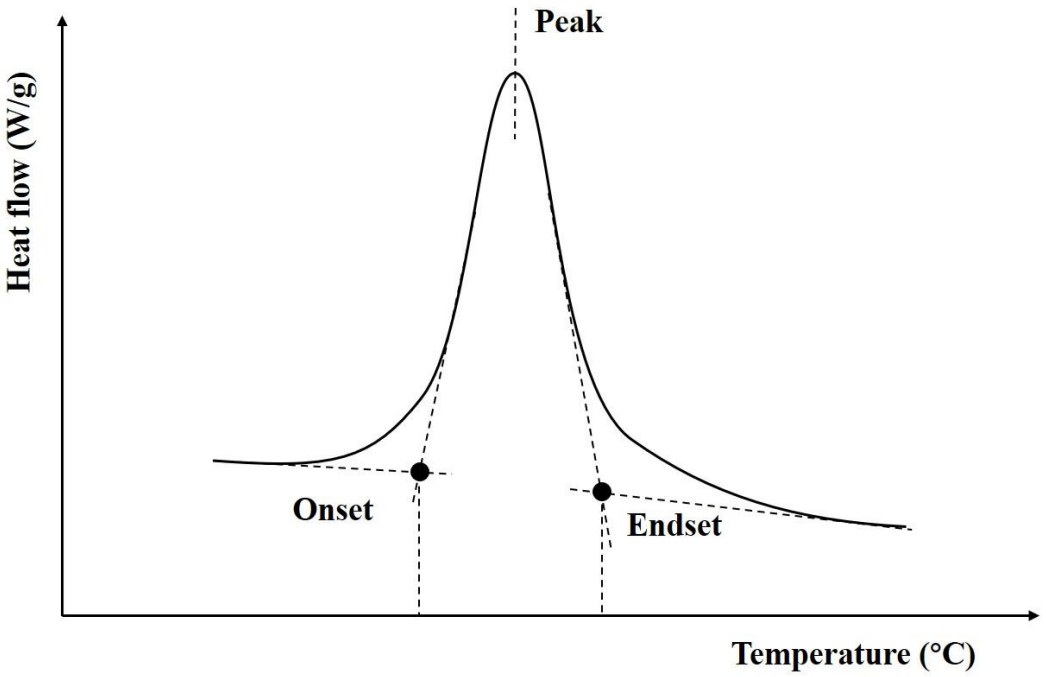

Fig. 2-6 Illustration of onset temperature T_{onset} in a specific peak on DSC thermogram.

2.4 Galvanostatic charge and discharge

Galvanostatic charge and discharge (GCD) is often used to determine the performance of an electrochemical system over time, simulating the real-world charging/discharging behavior of battery materials. It involves the application of constant positive and negative current to periodically charge and discharge an electrochemical cell, meanwhile the resulting potential is

recorded as a function of time. The cycles are repeated until a particular potential limit is reached. A number of key parameters can be derived from the GCD curves, including Coulombic efficiency (CE), capacity, possible presence of Faradaic reactions related with SEI formation or degradation, and state of health indicators such as polarization or overpotential, etc. The overpotential is a joint effect of several contributions, combining activation polarization, ohmic polarization (IR drop) and concentration polarization, as depicted in Fig. 2-7. The ohmic polarization is associated with the battery internal resistance (IR). The activation polarization arises from the energy barrier that must be overcome for electrochemical reactions to take place, for example, the charge transfer at the electrode/electrolyte interface. The dynamics of this process is described by the Butler-Volmer equation. The concentration polarization represents the voltage loss due to the fact that the rate of mass transfer is slower that the rate of reaction consumption itself. Overall, the higher the discharge rate is, i.e., larger current applied, the larger the overpotential becomes, meaning that the voltage curve shifts downwards in Fig. 2-7. Galvanostatic cycling could also specifically evaluate the stability and lifetime of the electrolyte materials using the symmetric cell configuration, which can be indicated by the cycling time before cut-off and the overpotential progression over time.

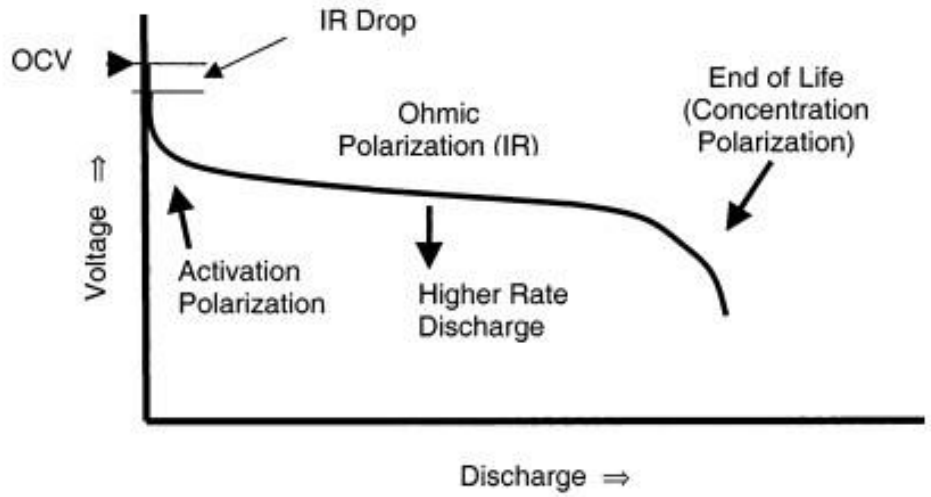

Fig. 2-7 Typical discharge curve of a battery, showing the influence of the various types of polarization [31].

3 Experimental

This chapter summarizes the details about the experimental procedures and parameters involved throughout this project, with the purpose to make them repeatable. The first section discusses the synthesis of materials, and the second section discusses the characterization methods.

3.1 Synthesis of the solid polymer electrolyte (SPE) membranes.

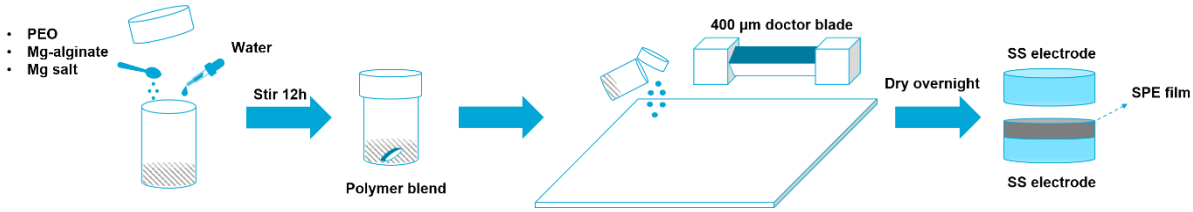

Fig. 3-1 Schematic of the synthesis process of solid polymer electrolyte membranes used for EIS test.

The solid polymer electrolyte was prepared by solution casting method, as shown in the above schematic (Fig. 3-1). Different amounts of PEO (average molecular weight: 100,000, *Sigma-Aldrich*), Mg-alginate (*BOC Sciences*), Mg salt (e.g., $MgCl_2 \cdot 6H_2O$, ACS reagent, *Sigma-Aldrich*) were dissolved in appropriate amount of demineralized water to produce a hydrogel solution after continuously stirring for 12 h at room temperature. The weight ratio of PEO to alginate was controlled ranging from 9:1 to 6:4, denoted as e.g., PEO90Alg10. The salt addition was taken as 20 weight percentage of the polymer solids altogether. The mixture was then cast onto a glass plate covered with a layer of PET film using a 400 µm doctor blade, and dried slowly in air to form peelable membranes. These were subsequently transferred to the desiccator and stored before any physicochemical and electrochemical measurement. The same protocol was also conducted for different salt types and different amounts of salt addition. Manufacturing details and parameters can be found in the appendix.

3.2 Characterization of SPE

In order to probe the structural and electrochemical properties of the as-synthesized SPE membrane, a variety of characterization techniques were performed, which include EIS, electronic conductivity measurement, XRD, DSC, and GCD.

3.2.1 EIS measurement

As previously explained, the ionic conductivity of the SPE can be determined by EIS technique. The electrolyte membrane was clipped to small disks using a 10 mm diameter punch to fit in

between the stainless-steel electrodes of a custom-made cell (see Fig. 3-2), which is specially designed for EIS measurements of solid-state batteries. It is composed of an insulating alumina hollow chamber which accommodates the sample and the upper and lower stainless steel outer shells. With the three screws manually tightened, the impedance spectra were then collected via the *Autolab PGSTAT302N* equipped with an *ECI10M* high-frequency module, and the supporting *Nova* software, where the AC frequency was programmed to range from to 10 MHz to 1 Hz with a voltage amplitude of 10 mV. A climate chamber (*Memmert UF30plus*) is also used in collaboration to realize high temperature measurements for example 60 °C. After assembly, the cell was put into the hot chamber and held for 5 mins before initiating the test. Conductivity at different temperatures were also evaluated for Arrhenius fits. The measurement was programmed as follows: the cell was kept at 30 °C for 1 h, then heated for 5 mins to 50 °C and maintained at this temperature for 30 mins. The process was proceeded to 90 °C by an increment of 10 °C, with 5 mins of heating and 30 mins of holding at each temperature step. The result obtained at the end of every 30-min-holding was chosen for the Arrhenius fits. All the gathered data was post-processed to fit the plots with the *ZView*® software. Fig. 3-3 shows an overview of the measurement set-up.

Fig. 3-2 Pictures of the solid-state cell used for EIS measurements after (left) and before (right) assembly.

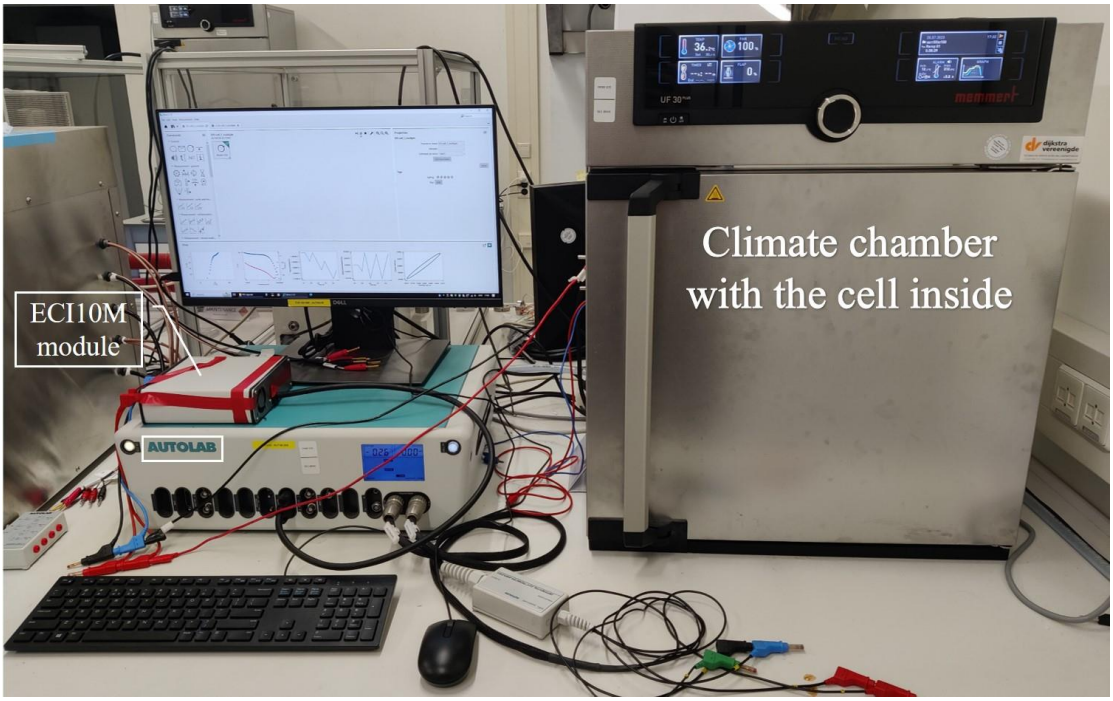

Fig. 3-3 Overview of the EIS measurement set-up.

3.2.2 Electronic conductivity measurement

To assess if the SPE has good electronic insulation ability. The electronic conductivity was measured with the multimeter by applying a constant DC voltage on the same assembled cell configuration as is used for the EIS measurements. The DC conductivity is calculated from the following equation, where R is the resultant resistance value from the multimeter, A is the area, t is the thickness:

$$\sigma_{DC} = \frac{t}{A \cdot R} \qquad (3-1)$$

3.2.3 X-ray Powder Diffraction

The SPE samples were analyzed on a X'Pert Pro X-ray Diffractometer (PANalytical) with a Cu K-α source (λ = 1.5406 Å) operating at 45 kV and 40 mA. The 2θ angle was scanned mostly over 5-60°. The intensity of the diffractive X-ray beam was measured against the 2θ angle. The room temperature measurement was done by simply placing the electrolyte membrane (or raw material powders such as PEO, alginate) on the open sample holder with the surface flat. In the case of elevated temperature measurement, the sample along with the sample holder were kept in the climate chamber at 60 °C for more than 1 h before testing. They were quickly transferred to the test spot with the sample still warm during the measurement, although the temperature was not necessarily 60 °C.

3.2.4 Differential scanning calorimetry

To study the thermal properties of the SPE membranes, the DSC thermograms were recorded in a commercial *TA-Q2000* DSC calorimeter equipped with a liquid nitrogen pumping system. Around 10 mg of crushed samples were loaded and sealed in aluminium pans. An empty pan was used as the reference. The scanning temperature spanned from 30 °C to 100 °C with a sweep rate of 10 °C/min. The data was processed in the supporting *TA universal analysis* software.

3.2.5 Galvanostatic charge and discharge

The galvanostatic charge/discharge cycling was performed in a symmetric cell set-up using the lab-cell model (see Fig. 3-4), which consists of the stainless-steel outer cases (#1), the rubber seal (#2), and the clamp (#3). The SPE membrane was sandwiched between two magnesium disks with a slightly smaller diameter (11.11 mm vs. 15 mm). The Mg electrode was polished with sand paper of 1500 and 2000 grits in sequence to remove the black oxidation layer, and then wiped with DME to erase any dirt and residue. The GCD test was performed on the *LANHE Battery Testing system* in combination with the climate chamber. The areal current density was 0.01 mA cm^{-2} and the charge/discharge time was 15 mins per cycle. The cell was rested long enough and then cycled at 60 °C until the voltage exceeded the pre-set safe limit (5V).

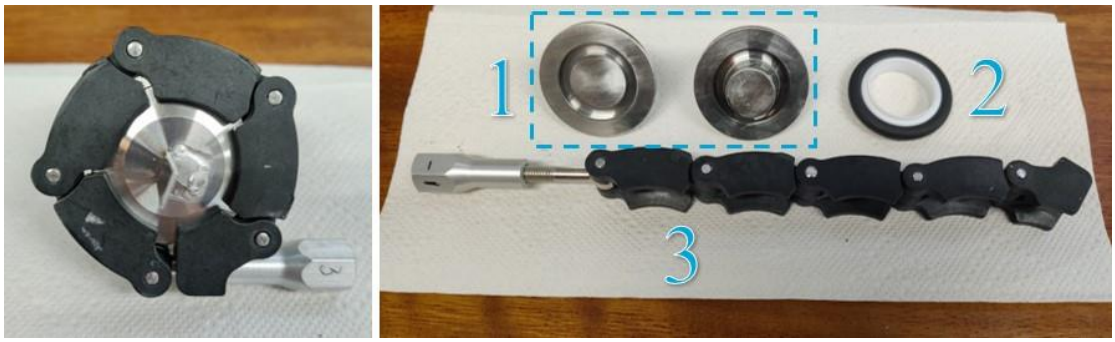

Fig. 3-4 Pictures of the lab-cell used for GCD cycling test after (left) and before (right) assembly.

4 Results and discussion

This chapter will summarize the results that were obtained based on the conducted experimental series. The results will be discussed to evaluate the feasibility of using the PEO – Mg-alginate polymer blend as ion conducting SPE. Some key insights will be presented to initiate the conclusions and recommendations in the upcoming chapters.

4.1 Synthesis of the SPE membranes

The electrolyte membranes appear free-standing featured with good flexibility, as shown in Fig. 4-1. However, the mechanical properties are greatly affected by the content of alginate and salt in the mixture with a certain limit. We cannot get a flexible and peelable membrane with excessive amount of alginate or salt. Detailed conditions will be elaborated in discussions about the conductivity results. The original appearance of the freshly made electrolyte membrane is opaque with visible crystals and sometimes pores are present on its surface (Fig. 4-1 (a)). After resting at high temperature for a while, the membranes become transparent or semi-transparent, as seen from Fig. 4-1 (b). In-depth analysis about this transition will be explored afterwards. The thickness of fully dried sample is around 80 ~ 120 μm. Besides, the electronic conductivity results have suggested that this SPE possesses a negligible DC conductivity, which is desirable for a solid electrolyte.

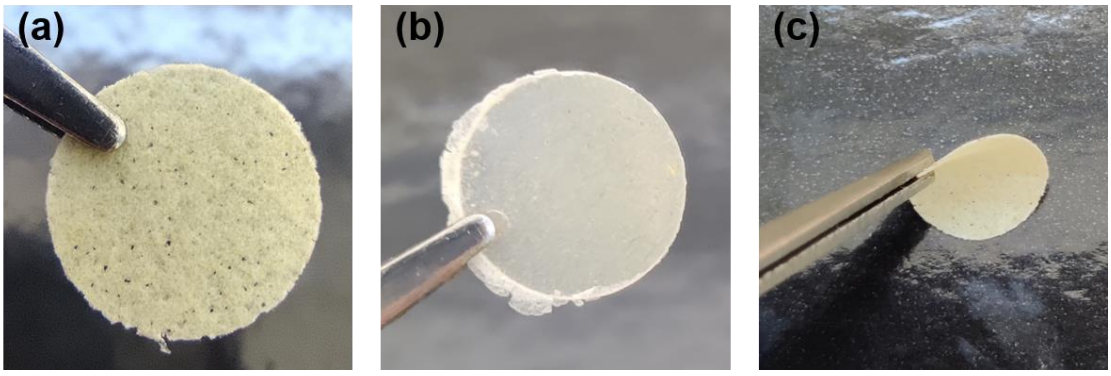

Fig. 4-1 Pictures of the solid polymer electrolyte (SPE) free-standing membrane. (a) Original appearance before EIS measurements. (b) Appearance after EIS measurements at 60 °C. (c) Picture showing the good flexibility of this SPE material.

4.2 Ionic conductivity

Based on literature review, it is well known that the ionic conductivity is greatly influenced by several composition parameters such as the salt type and concentration, the property of the polymers and their ratio [12]. In this section, we controlled different polymer ratio, different magnesium salt and concentration to optimize the SPE composition with a favorable ionic conductivity.

4.2.1 Variation of the alginate content in PEO – Mg-alginate – $MgCl_2 \cdot 6H_2O$ system

Before adding any Mg-alginate, the conductivity of PEO mixed with 20 wt.% $MgCl_2 \cdot 6H_2O$ was tested at 60 °C, resulting in a negligible value of ~10^{-9} S·cm^{-1} which is in consistent with the previously reported value [32]. Then electrolyte films with alginate concertation up to 40 wt.% of the whole polymer and 20 wt.% (based on the polymer weight) $MgCl_2 \cdot 6H_2O$ addition were prepared. The film could not be successfully peeled off when the amount of Mg-alginate reached 50 wt.%. The impedance spectra for each composition tested at 60 °C are shown in Fig. 4-2 (a). These Nyquist plots all look as expected in the previous chapter 2.1, which exhibit an arc on the real axis followed by a diffusion-controlled tail at low frequencies. The diameter of the semicircle gradually decreases with the increase of alginate content. Since for the initial stage, the ionic conductivity is what we are most interested in, the first region of the curve was exclusively fitted using the proposed model in chapter 2.1. The ionic conductivities were calculated according to Eq. 2-3, and the results were plotted against the alginate concentration depicted in Fig. 4-2 (b). From the line chart we can observe that the conductivity is steadily increased as the content of alginate goes up. This is probably because of the introduction of Mg-alginate brings about more charge carriers i.e., Mg^{2+} and more coordination sites for ions hopping, given that conductivity is a function of the number of charge carriers (n), and their mobility (μ), as defined by the following equation:

$$\sigma = n \cdot q \cdot \mu \qquad (4-1)$$

where, q is the amount of charge. As previously pointed out the potential conduction properties of alginate, the Mg-ions are loosely bound with the COO^- groups of alginate and can freely move to the next empty site either on PEO or on alginate chain, which causes the boost of mobility. Also, the crystallinity of PEO could be possibly reduced to provide another way of increasing ion mobility owning to the blending between the two polymers. The increased amorphous phase enlarges the free volume which can offer more pathways for ion transport. However, this is yet to be confirmed by XRD which will be discussed later. The maximum conductivity can be obtained from the sample PEO60Alginate40 with 20 wt.% Mg salt, showing a value around 1.5 × 10^{-6} S·cm^{-1}, which is rather mediocre considering that room temperature conductivity ranging from ~10^{-5} to ~10^{-4} S·cm^{-1} has already been achieved for PEO-based Mg^{2+} conducting SPE [33], [34]. However, it is worth mentioning that the result is obtained only after 5 mins of holding in the hot chamber before starting the measurement program. Actually, there exists a direct correlation between conductivity and holding time due to the fact that the SPE needs an additional activation process to achieve an optimal conductivity. This will be extensively discussed in chapter 4.2.4.

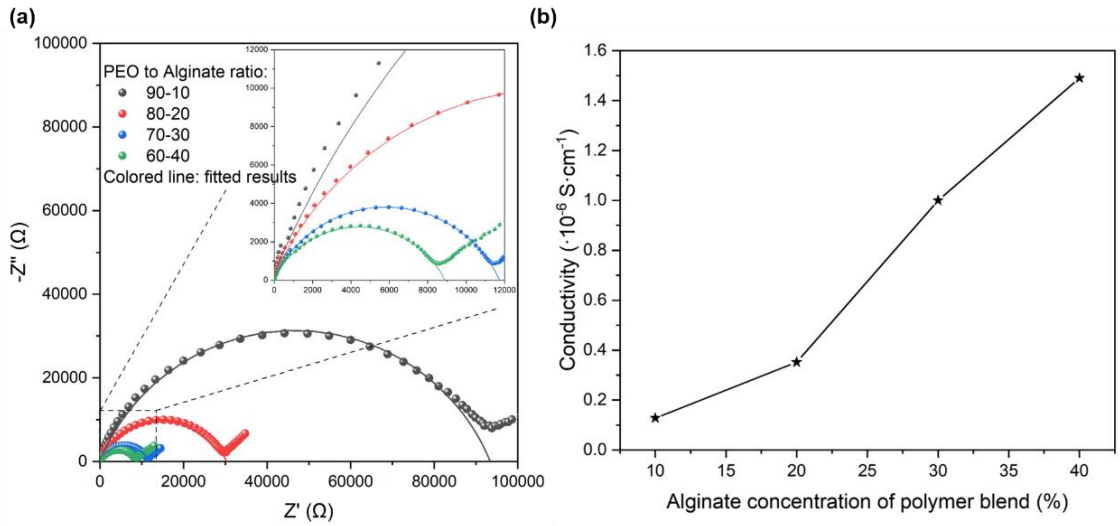

Fig. 4-2 (a) Impedance spectroscopy analysis for SPE samples with different PEO – Mg-alginate ratios. (b) The relation between conductivity and variation of alginate concentration.

4.2.2 Influence of different $MgCl_2$ concentration

The best performing combination of varying amounts of PEO and Mg-alginate (PEO60Alg40) was chosen to further investigate the effects of difference in salt concentration on conductivity. The doping concentrations of $MgCl_2 \cdot 6H_2O$ included 5, 10, 15, 20 wt.%. When attempting to add 25 wt.%, we cannot get intact film because the inclusion of more salt destroyed the flexibility of the polymer matrix. The EIS results and conductivity plotted as a function of salt concentration are presented in Fig. 4-3. Similarly, the diameter of the semi-circle in high frequency decreases with increasing salt amount. It can also be observed that the highest conductivity is still the sample of PEO60Alginate40 with 20 wt.% of $MgCl_2$. The increase in conductivity experiences a minimal increment from 5% to 10% $MgCl_2$ and then a sharp rise from 10% to 20%. Although extra salt content can always bring about more charge carriers, only mobile charge carriers can positively contribute to conductivity. Thus, the increase in salt content does not necessarily lead to the continuous improvement in conductivity. The additional ions come to bond with the polymer coordination sites and form polymer-salt complex which restricts their migration at low doping level [35]. Afterwards, the value is increased eightfold to 1.5×10^{-6} S·cm^{-1} by doubling the salt addition from 10 to 20 wt.%, which is the real effect from the build-up of mobile charge carriers in the system. According to the breathing chain model, the segmental motions of polymer such as opening and folding of the chains are accompanied with a change in free volume [35]. These microscopic movements can help with the disassociation of salts and thus result in a greater number of mobile charge carriers with enhanced mobility. It is also reported that this kind of curve can have a saturated value of conductivity due to that fact that excessive salt content can cause ion pairs and ion aggregates formation [34]. However, in this research, the poor mechanical quality of electrolyte membranes as a result of too much salt comes before this potential turning point.

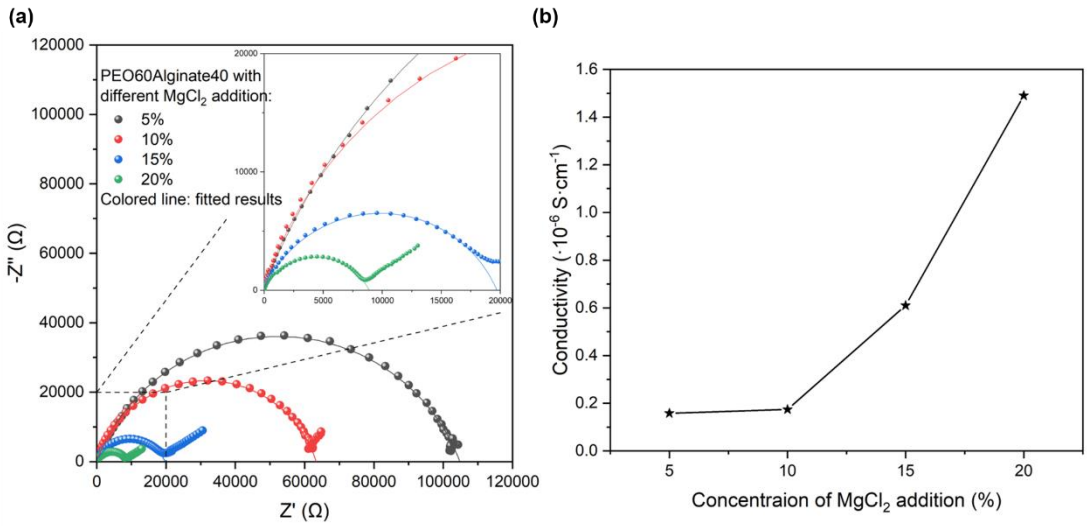

Fig. 4-3 (a) Nyquist plots of SPE samples with different $MgCl_2$ addition. (b) The variation of ionic conductivity of SPE membranes with $MgCl_2$ concentrations.

4.2.3 Temperature correlation of ionic conductivity

Once again, the PEO60Alg40 with 20 wt.% $MgCl_2 \cdot 6H_2O$ doping sample with the highest conductivity was used to study the variation of conductivity as a function of temperature in the range of 323 ~ 363K. It can be seen from Fig. 4-4 that this solid polymer electrolyte obeys the rule of Arrhenius behavior. The conductivity is linearly correlated with the inverse of temperature. The obtained values for conductivities at different temperature is shown in Table 4-1. The sample shows a conductivity of around 6.2×10^{-5} S·cm^{-1} at 70 °C and rises up to ~10^{-4} S·cm^{-1} above 80 °C, which is comparable to some reported values but not making it to the first tier [36], [37]. It is also found that the conductivity goes through the first drastic increase from 60 to 70 °C. Very likely that is temperature range where the melting temperature of crystalline phase (T_m) locates. This can be further determined by DSC, which will be discussed in chapter 4.4. From T_m upwards, the SPE behaves like gel polymer electrolyte which has a good mobility leading to the excellent conductivity. As discussed in chapter 1.4, the Arrhenius behavior indicates that the ion conduction primarily originates from the ion hoping among vacant coordination sites provided by PEO and alginate since they have a significant number of functional groups. As temperature increases, the ion gains enough energy to overcome the potential barrier of hopping, leading to increased mobility and thus improved conductivity. Although the polymer segmental motion is also augmented at elevated temperature which can produce larger free volume favorable for ion transport, it is not considered to be the prevailing effect that dominates the process. Applying the Arrhenius equation in Eq. 1-1 to fit the plot, the activation energy can be calculated to be 1.77 eV. It should be recognized that this value is a lot larger compared to the literatures which all similarly study the Mg^{2+} conducting polymer blend electrolytes e.g., 0.33 eV in PEO-PVP [34], 0.3 ~ 0.7 eV in PVA-PVP [38], and 0.21 eV in PVA-PAN [39]. This notable amount of activation energy means large potential barrier to overcome for ion hopping, suggesting the unfavorable transport properties of this electrolyte material.

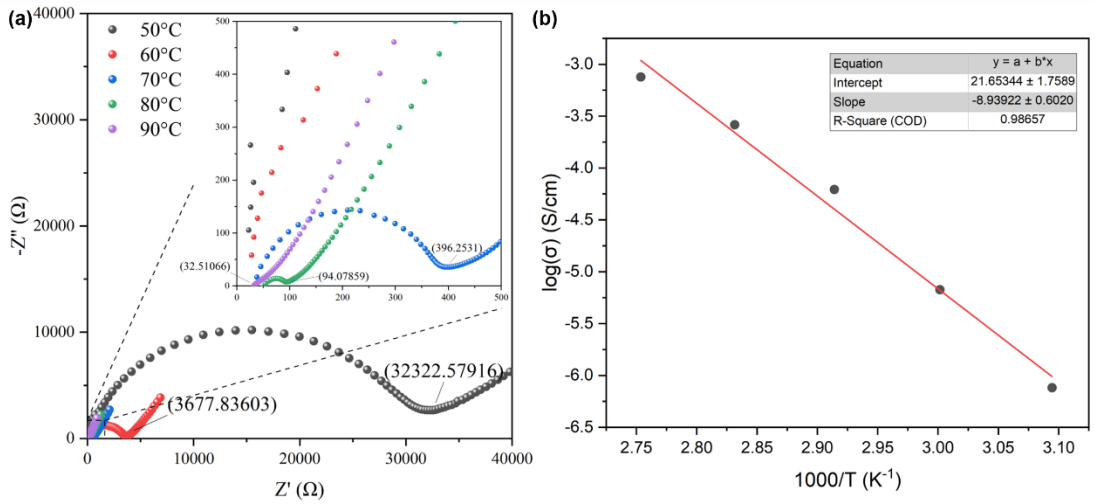

Fig. 4-4 (a) Nyquist plots of one sample of particular composition (PEO60Alg40) at different temperatures. (b) Temperature correlation of ionic conductivity generated based on the EIS results.

Table 4-1 Calculated conductivities for PEO60Alg40 plus 20 wt.% $MgCl_2$ at different temperatures.

Temperature (°C)	Conductivity ($\cdot 10^{-5}$ S/cm)
50	0.076
60	0.67
70	6.19
80	26.09
90	75.5

4.2.4 Effects of the testing parameters

Actually, the heating time makes nonnegligible impacts on the obtained conductivity results. The earlier stated 5 minutes is thought to give samples and cells enough time to warm up, which was selected mainly for the convenience and efficiency of test. In fact, the holding time before measurement can be regarded as a process of heat treatment with the applied pressure from the warm stainless-steel electrodes, which is identical to the hot pressing. To understand the importance of the holding process, non-stopping multiple EIS measurements have been conducted immediately after well positioning the cell, during which the impedance has been recorded with respect to cycles, as shown in Fig. 4-5. The test was performed at 60 °C and the reason for choosing this temperature was that it was close to the melting temperature of PEO, ensuring an optimal conductivity, while the sample still retained solid state. This reason is also applicable for the rest measurements involved in this research. The sample composition chosen for testing was still PEO60Alg40 with 20 wt.% $MgCl_2 \cdot 6H_2O$. It can be noticed that the diameter of the semicircle at first decreases with time then stops at a certain point, which means the conductivity keeps increasing until a saturated value of 1.05×10^{-5} S·cm^{-1} after around 8 cycles of measurement. The evolution of conductivity seems to have gone through an activation process, which can also be supported by the disappearance of the crystals and clusters previously present in the electrolyte membrane (Fig. 4-1 (a) (b)). Similar phenomenon is also

reported elsewhere, where the heat treatment can remove the formed crystal structures during the drying of PEO-based SPE [19]. This process is considered due to the disassociation of salts as the sample temperature gradually goes up to the set value of the climate chamber. Based on the breathing chain model, microscopically, the polymer chain is relaxed and segmental motion is enhanced at an elevated temperature, resulting in the free volume change, which induces the disassociation of salts and upsurge of mobile charge carriers. The salt could also be uniformly re-distributed during heating, accelerating the activation process.

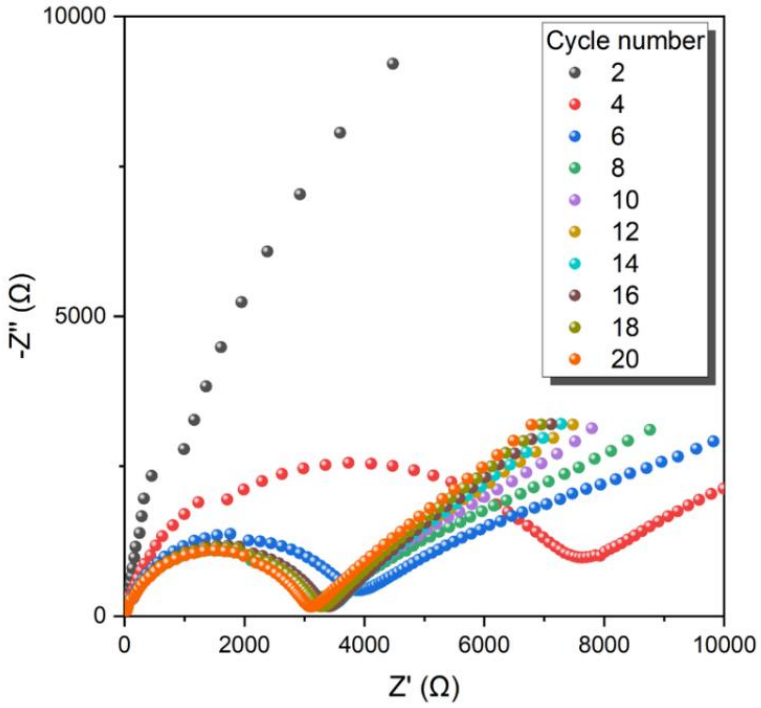

Fig. 4-5 Nyquist plots with respect to cycles showing the effects of holding time.

4.2.5 Adoption of different salt

Apart from $MgCl_2 \cdot 6H_2O$, other salts were also employed to explore the effects of salt type on the conductivity of SPE, including $MgSO_4$ and $Mg(ClO_4)_2$. The results are discussed hereinafter. They are not very comprehensive to cover every aspect, but still are shown here to provide some general insights.

I. $MgSO_4$

Magnesium sulfate ($MgSO_4$) was the first salt used to replace $MgCl_2 \cdot 6H_2O$ in PEO – Mg-alginate copolymer system. However, $MgSO_4$ leads to the salting out of alginate seriously, as seen from the photograph taken during the synthesis attempt Fig. 4-6. Homogenous aqueous solution could not be achieved as the alginate formed flocculent agglomerates. This is because the high charge density SO_4^{2-} is a kosmotropic (means order-making) anion which can stabilize the hydrogen-bonding network of water molecule and compete with water to form ion pairs with cations in the cation solvation process [40]. This effect can also remove water from

the polymer network thus resulting in polymer precipitates and more free water. Practically, the sulfates are often used as agents to salt out proteins from aqueous solution due to this effect. Therefore, $MgSO_4$ is deemed impractical in using as a salt source for Mg-ion conducting polymer electrolytes. There is also no realization of this in the literature, as deduced from Table 1-1.

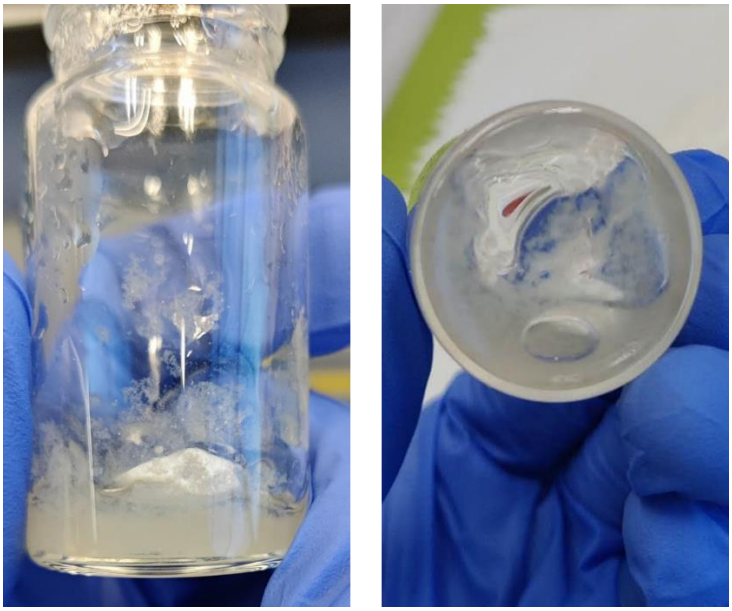

Fig. 4-6 Photograph showing the effect of alginate aggregation and salting out caused by $MgSO_4$.

II. $Mg(ClO_4)_2$

In light of this, a less kosmotropic agent, that is to say more chaotropic, is of great interest. According to the empirical Hofmeister series (see Fig. 4-7), ClO_4^- sits on the most right end of the order owing to its low charge density, which implies its ability to increase the solubility of the solute in the system [40]. Thus, $Mg(ClO_4)_2$ was selected to fabricate the electrolyte membranes. The PEO with varying alginate content were mixed with 5 wt.% of $Mg(ClO_4)_2$ and casted. However, the previous thickness could not ensure good quality of the membranes in terms of using $Mg(ClO_4)_2$. So thicker membranes were made with a doctor blade of 1 mm thick to be able to incorporate only 5 wt.% of $Mg(ClO_4)_2$ (10 wt.% only possible with pure PEO and no alginate). The EIS measurement results are presented in Fig. 4-8. Overall, around 10^{-4} $S \cdot cm^{-1}$ was achieved for all samples, including pure PEO doped with $Mg(ClO_4)_2$. The value for the latter composition was an order of magnitude higher than the literature, where shows a conductivity of ~10^{-5} $S \cdot cm^{-1}$ at 60 °C for $(PEO)_9Mg(ClO_4)_2$ [41]. This may be because the previous drying time was not long enough to remove all the residual water due to the increased sample thickness and strong water absorption property of $Mg(ClO_4)_2$. As stated in chapter 1.5, higher water content provides an additional medium to ions to migrate and decreases the crystallinity of SPE, thus enhancing the ion mobility. However, it is undeniable that part of the contributions could come from the intrinsic nature of $Mg(ClO_4)_2$ which possesses a low lattice energy thanks to the low charge density of ClO_4^-. Regardless of the numbers, the ionic conductivity shows a trend of firstly increasing with larger alginate amount to a saturated value

then decrease sharply. Similar to what has been accounted for $MgCl_2$, the variation is attributed to the interplay of the increasing mobile charge carriers in competition with immobilized ion pairs and aggregates because of ions interactions.

Fig. 4-7 Hofmeister anion series indicating the ability to stabilize water-water interactions with the strong water-stabilizing kosmotropes on the left and chaotropes on the right end of the series [40].

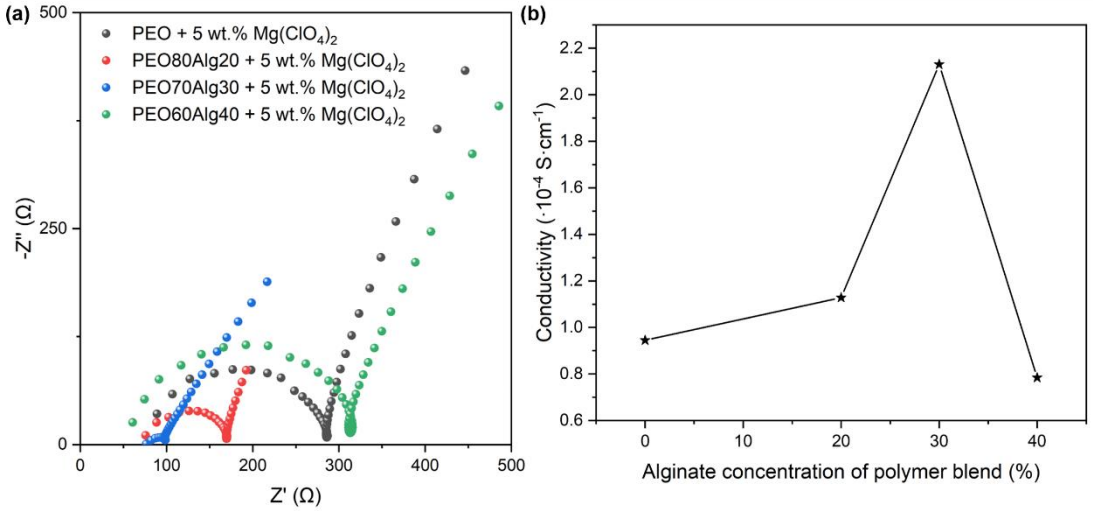

Fig. 4-8 (a) Nyquist plots for SPE samples with varying alginate content blended with PEO and 5 wt.% of $Mg(ClO_4)_2$. (b) Conductivity plotted versus alginate concentration.

4.3 Structural analysis based on XRD

To begin with, the raw materials were used and examined as they were received. It was interesting to find out that the Mg-alginate was not 100% pure, with MgO impurity which is a manufacture byproduct according to the supplier (Fig. 4-9). Pure alginate should be totally amorphous with broad diffraction band, absent of the sharp peaks of 2θ angles at around 43° and 63°. The role and behavior of MgO will be involved in the following discussions. Semi-crystalline PEO exhibits two intense peaks at around 19° and 23° and a minor peak at 27°, corresponding to (1 2 0), (1 1 2) and (2 2 2) planes respectively (see Fig. 4-10) [42].

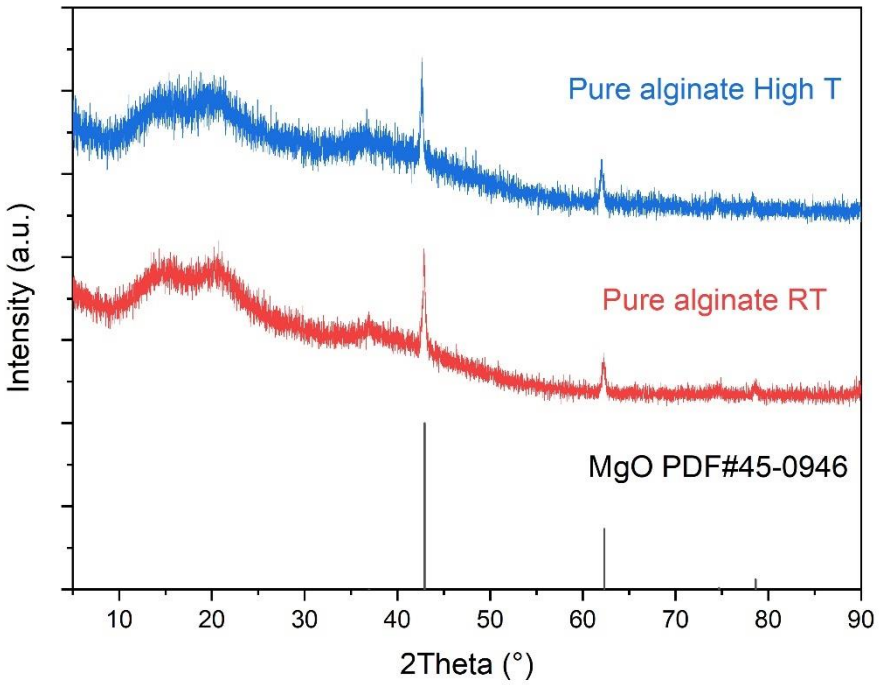

Fig. 4-9 XRD diffraction pattern of pure Mg-alginate at room temperature and elevated temperature.

Normalized XRD diffraction pattern with respect to the most intense peak of different alginate incorporation content tested at room temperature is shown in Fig. 4-10. First of all, there is no obvious peaks of $MgCl_2$ or its hydrate present in each pattern, which represents the complete dissolution and coordination of the salt. It can also be observed that every composition shows a similar pattern, with the two most intense peaks of PEO crystalline phase as well as the MgO characteristic peak of alginate. This implies that no interaction between PEO and alginate is formed. If there was any interaction of PEO and other polymer such as crosslinking or grafting effect, either the second strongest characteristic peak of PEO (at 19°) or both peaks would disappear and combine as a new peak as reported in the literature [34], [36]. This means the crystalline phase of PEO is disturbed and the micro-structure is rebuilt. However, such changes did not appear in this copolymer system. Looking into the XRD patterns obtained at high temperature in Fig. 4-11, the only difference is that for some compositions, the peak intensity of MgO is reduced at high temperature and increases back after completely cooling down to room temperature. We assume that this is because the mobility of polymer and other species is enhanced at high temperature, which causes the well dispersion of MgO. It becomes less concentrated thus difficult to be detected, resulting in a less intense peak.

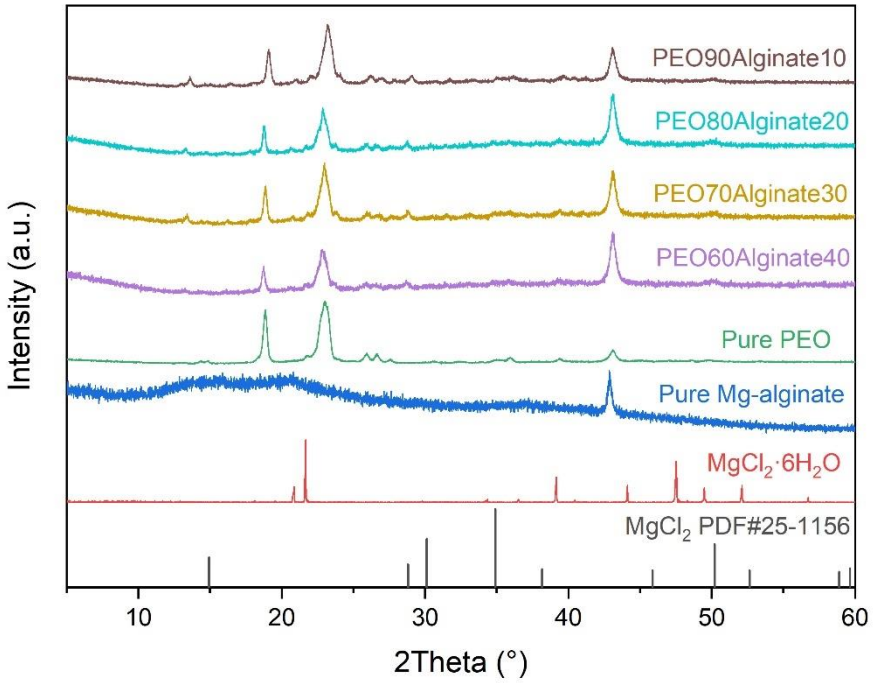

Fig. 4-10 Room temperature XRD diffraction pattern of SPE samples with varying PEO to alginate ratio (with 20 wt.% $MgCl_2$ addition).

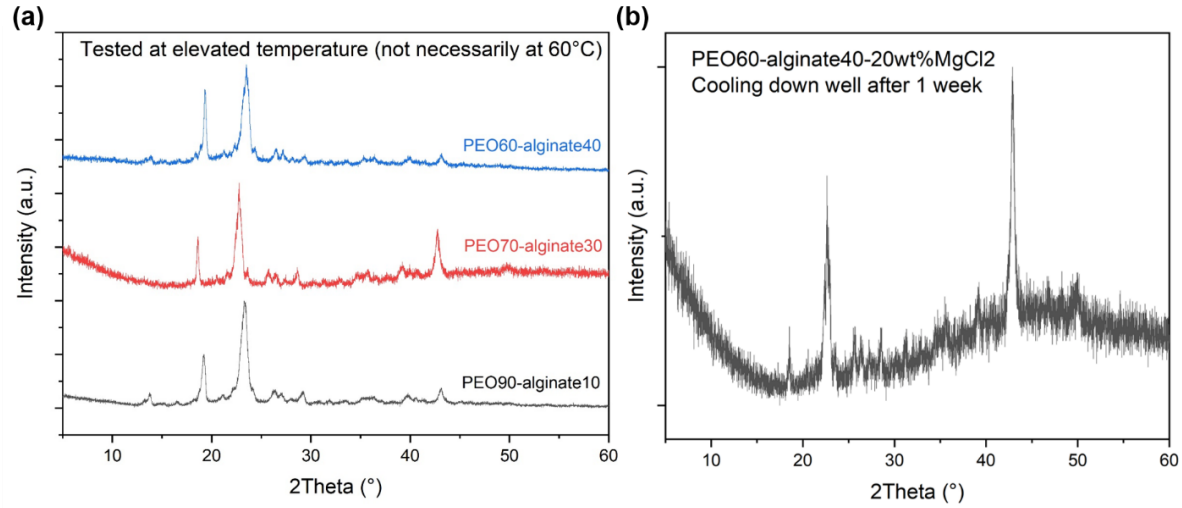

Fig. 4-11 (a) XRD pattern of samples with different alginate incorporation tested at an elevated temperature. (b) one particular sample tested after cooling down to room temperature

From the above discussion, it could be concluded that the salt does not contribute to the reconstruction of the structure at all, at least for the addition concentration of 20 wt.% below. Therefore, to find out more information about the possible effects of salt addition, a doubled concentration of 40 wt.% was made with a higher membrane thickness to support the composition change. Results are shown in Fig. 4-12 (a). The patterns are again pretty much similar with no big alterations in terms of the primary peaks and the only difference is that the

XRD pattern with more salt shows more noisy signals. This could be due to the salt are not completed dissolved. Changing the salt type to $Mg(ClO_4)_2$ also results in the similar outcome, as seen from Fig. 4-12 (b).

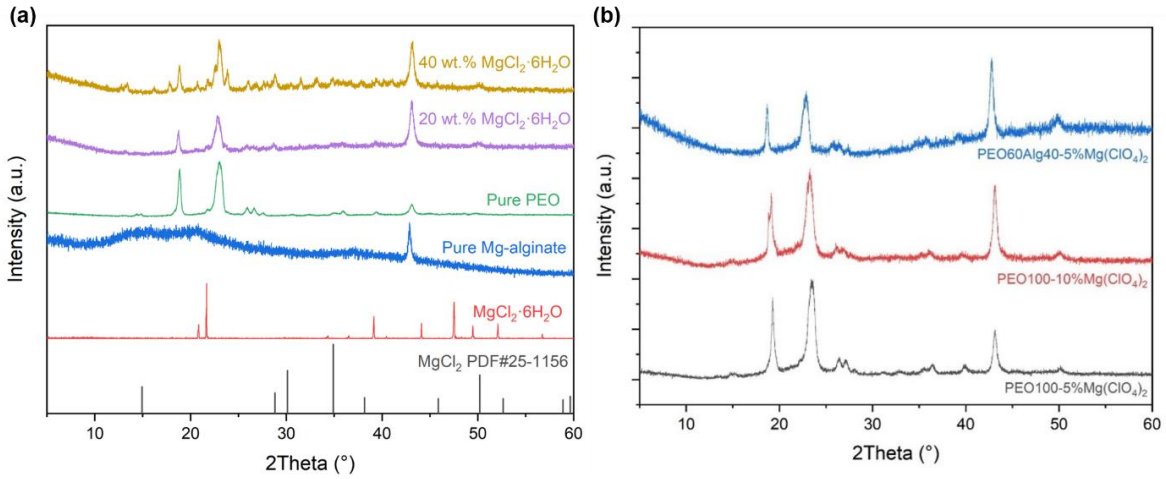

Fig. 4-12 Room temperature XRD diffraction of SPE samples (a) with different $MgCl_2$ content. (b) with different salt type.

4.4 Thermal analysis based on DSC

The DSC results are presented down below, see Fig. 4-13. Due to the limitation of the DSC instrument that is used, the lowest temperature of measurement could only start from 30 °C. Thus, the glass transition could not be recorded since the SPE is expected to have a well below zero glass transition temperature predicted from its PEO host matrix. As observed from the thermograms, two scans were conducted on two samples with bipolar compositions (PEO90Alg10 and PEO60Alg40), exhibiting evident melting and recrystallization peaks. The melting peak for the first scan is slightly larger than the second in both cases, which is maybe because additional heat is needed in the first cycle such as the disassociation of the salt. Additionally, after melting, the sample also achieves a better contact with the bottom of the crucible, resulting in a lower thermal resistance. Thus, the second scan is considered more stable and subsequently used to analyze the thermal parameters. The melting temperature can be characterized either with the onset temperature or the peak temperature which are listed in Table 4-2 for each composition. Slight deviations of the melting temperature were found comparing both compositions, indicating the alginate does not affect T_m too much since it is fully amorphous with no precise T_m. In any case of T_{onset} or T_{peak}, the melting temperature lies in the range of the whole melting peak around 60 ~ 70 °C, which is in agreement of the transition point of conductivity with respect to temperature as described in chapter 4.2.3.

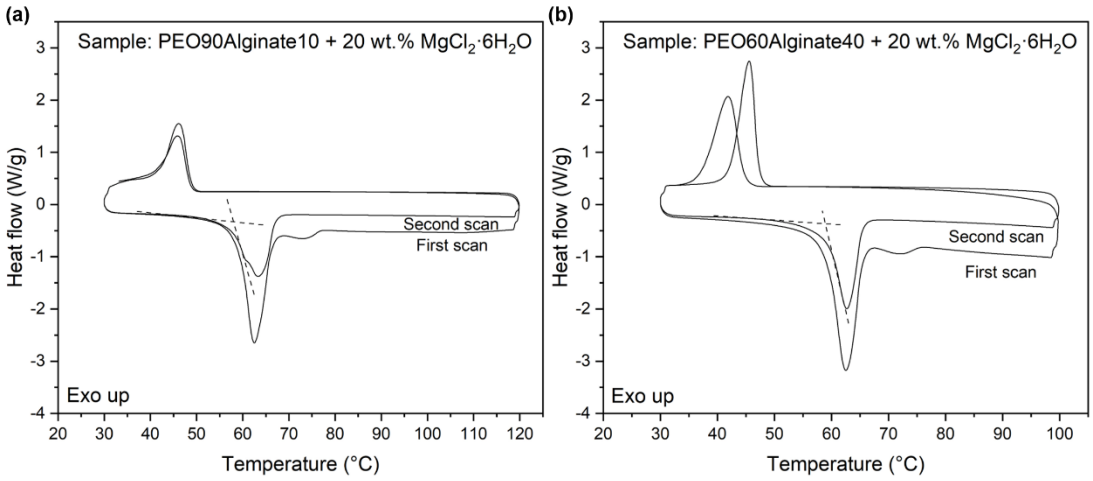

Fig. 4-13 DSC thermograms of two samples with different composition. (a) PEO90Alginate10 + 20 wt.% $MgCl_2 \cdot 6H_2O$. (b) PEO60Alginate40 + 20 wt.% $MgCl_2 \cdot 6H_2O$.

Table 4-2 Comparison of the melting onset temperature and peak temperature.

Sample composition	Melting onset temperature (T_{onset}) (°C)	Melting peak temperature (T_{peak}) (°C)
PEO90Alginate10 + salt	58.78	63.18
PEO60Alginate40 + salt	59	62.66

4.5 Galvanostatic cycling

Although various Mg^{2+}-conducting solid polymer electrolytes have been synthesized and reported about their conductivities, few of them looked into the reversibility of Mg stripping/plating. Besides favorable ionic conductivity, the compatibility against Mg metal is also an indispensable property to achieve full cell application for SPE materials. To evaluate the cyclability of our PEO – Mg-alginate – $MgCl_2$ SPE membranes with the best performing composition, galvanostatic cycling test was conducted using the magnesium symmetric cell configuration. Despite featured with a modest conductivity as shown before, surprisingly, this material (PEO60Alginate40 + 20 wt.% $MgCl_2 \cdot 6H_2O$) could support over 300 cycles (150 h) until cut-off at the safe voltage limit. The first 100 h is extracted and plotted in Fig. 4-14, where representative cycles are selected, showing the overpotential evolution. Overall, the voltage profile is rather stable in such period of time. It also exhibits a neck, i.e., the overpotential increases at first and then experiences a stage of decrease before increasing again to the failure of the cell. This phenomenon has also been observed in another cell (results are shown in the Appendix). This could suggest the improvement of Mg dissolution and deposition at a certain point during cycling. To gain more information about the exact mechanism, further surface analysis in the future could help with determining the surface composition to see if there is any Faradaic reaction product that can stabilize the reversibility of Mg stripping/plating. The deposition/stripping overpotentials were observed to be $\leqslant$ 0.25 V for the first 50 cycles with the low value around 0.1 V. After the necking phenomenon at around 100 cycles, the overpotential decreased back to this value and maintained for another 50 cycles. Even the

largest value is no more than 0.4 V during the course which is comparable to the literature although a smaller current density is applied in our case [43]. However, the discharge plateau is not very smooth with obvious fluctuations, indicating the instability of the deposition process.

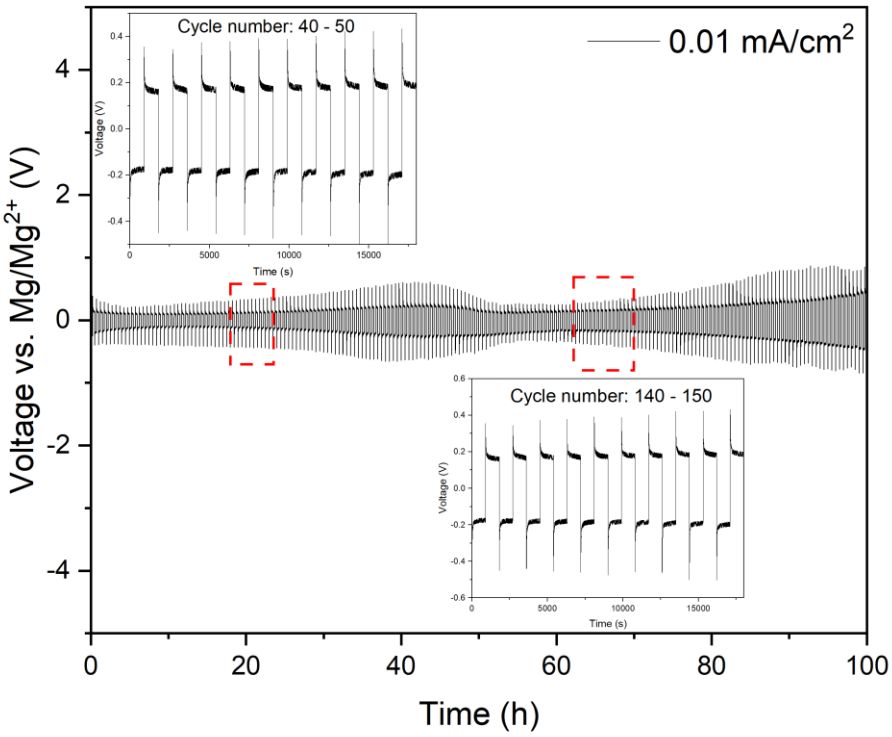

Fig. 4-14 Galvanostatic cycling for symmetric Mg||SPE||Mg cell carried out at 0.01 mA/cm^2 with the charge/discharge time of 0.25 h.

4.6 Possible transport mechanism of the PEO – Mg-alginate – $MgCl_2$ system

Based on the above discussion, the transport mechanism of this solid polymer electrolyte could be generally pictured as drawn in Fig. 4-15. It is Arrhenius behavior dominated meaning that the SPE conducts by ions hopping among the vacant coordination sites. The PEO and alginate offer two individual sets of coordination sites pending to be bound with ions respectively, with no interaction in between the polymers. Under an applied electric field, the ether group (-O-) of PEO is polarized and forms dipoles which can bond with cations, while the alginate forms liable metal-ligand bond with Mg^{2+}, which is described as diffusively bonding by some researchers. Therefore, Mg^{2+} could move intra-molecularly within each polymer chain as well as inter-molecularly to another polymer chain, realizing the transport of charge. Although ideally it is thought only Mg^{2+} being transported and conducted, the real case is very complex as the anions could also participate in the process. The transference number could be determined by further investigations on this system to identify the real contribution.

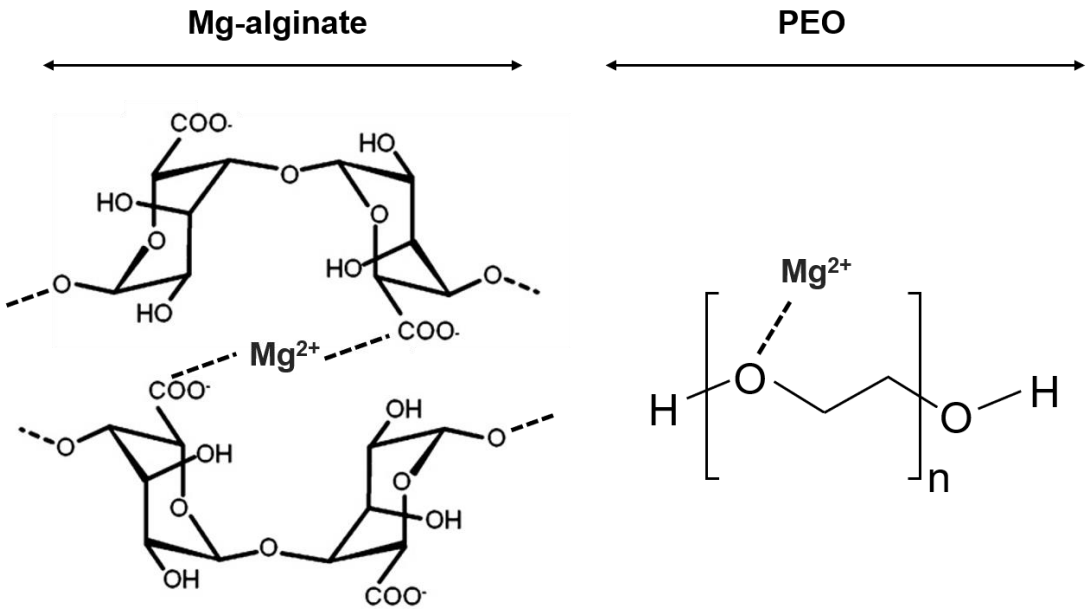

Fig. 4-15 Idealized ion conduction model for the PEO – Mg-alginate – $MgCl_2$ system.

5 Conclusion

Throughout this research, solid polymer electrolytes composed of PEO, Mg-alginate and $MgCl_2$ have been successfully prepared. A number of synthesis parameters have been optimized, including different polymer ratio, different salt type and concentration. The following conclusions could be drawn based on the results of materials characterization analysis:

(1) Free-standing electrolyte membranes with different compositions were obtained. The best conductivity is achieved in the sample of PEO60Alginate40 with 20 wt.% of $MgCl_2 \cdot 6H_2O$, exhibiting a value of 1.5×10^{-6} $S \cdot cm^{-1}$ at 60 °C. However, this value originates from only 5 mins of holding in the climate chamber. The ionic conductivity is expected to be further improved by extending the holding time at high temperature.

(2) The holding time before EIS measurement has a direct impact on the ionic conductivity. There is an activation process before the electrolyte membrane reaches the saturated value of conductivity around 10^{-5} $S \cdot cm^{-1}$ at 60 °C.

(3) The copolymer-based SPE membrane shows an Arrhenius behavior with respect to temperature, which indicates the ion conduction is dominated by ion hopping. During the test, the membrane achieves a conductivity of $\sim 10^{-4}$ $S \cdot cm^{-1}$ at 80 °C and above. However, the calculated activation energy is as high as 1.77 eV which suggests the high potential barrier of ion transport.

(4) The XRD results indicate that there is no interaction in between PEO and Mg-alginate. The PEO still shows a high degree of crystallinity after the inclusion of Mg salt and alginate. The main function of PEO is to provide another medium of ion hopping and account for the mechanical strength and flexibility of the electrolyte film.

(5) Galvanostatic cycling of symmetric Mg battery shows excellent cycling stability up to 150 hours (300 cycles). It seems that the reversibility of Mg stripping/plating is improved during the cycling process. Further investigations on the surface composition are needed to gain more insights.

(6) A relevant ion conduction model is built within the system. PEO and alginate provide two sets of coordination sites for ion hopping respectively.

By now, the research question can be answered. Although PEO and alginate are considered not a very good combination of copolymer-based SPE since no interaction is formed in the mixture, it still managed to show a conductivity of above 10^{-5} $S \cdot cm^{-1}$ from 60 °C upwards and an excellent cycling stability, calling for more in-depth attention towards this topic.

6 Recommendations

Further research could be conducted in the following directions:

(1) Check the morphology and composition of the Mg metal/SPE interface during cycling to determine if there is any specific layer formed which can stabilize the Mg dissolution/deposition.

(2) Determine the transference number T_+ by Evans method to see if the SPE is dominated by cationic or anionic transport.

(3) Substituting PEO with another polymer with functional groups that can interact with the carboxyl (COO^-) or ether (-O-) groups of Mg-alginates. Examples of possible polymers include poly(vinyl alcohol) (PVA) with hydroxyl group, poly(vinylidene difluoride) (PVDF) with fluorine group thus forming hydrogen bonding between the polymer backbones.

Bibliography

[1] H. Kim, G. Jeong, Y.-U. Kim, J.-H. Kim, C.-M. Park, and H.-J. Sohn, 'Metallic anodes for next generation secondary batteries', *Chem. Soc. Rev.*, vol. 42, no. 23, pp. 9011–9034, 2013, doi: 10.1039/C3CS60177C.

[2] Y. Wang *et al.*, 'Emerging non-lithium ion batteries', *Energy Storage Mater.*, vol. 4, pp. 103–129, Jul. 2016, doi: 10.1016/j.ensm.2016.04.001.

[3] C. Wei, L. Tan, Y. Zhang, Z. Wang, J. Feng, and Y. Qian, 'Towards better Mg metal anodes in rechargeable Mg batteries: Challenges, strategies, and perspectives', *Energy Storage Mater.*, vol. 52, pp. 299–319, Nov. 2022, doi: 10.1016/j.ensm.2022.08.014.

[4] H. Deog Yoo, I. Shterenberg, Y. Gofer, G. Gershinsky, N. Pour, and D. Aurbach, 'Mg rechargeable batteries: an on-going challenge', *Energy Environ. Sci.*, vol. 6, no. 8, pp. 2265–2279, 2013, doi: 10.1039/C3EE40871J.

[5] Z. Ma, D. R. MacFarlane, and M. Kar, 'Mg Cathode Materials and Electrolytes for Rechargeable Mg Batteries: A Review', *Batter. Supercaps*, vol. 2, no. 2, pp. 115–127, Feb. 2019, doi: 10.1002/batt.201800102.

[6] R. Deivanayagam, B. J. Ingram, and R. Shahbazian-Yassar, 'Progress in development of electrolytes for magnesium batteries', *Energy Storage Mater.*, vol. 21, pp. 136–153, Sep. 2019, doi: 10.1016/j.ensm.2019.05.028.

[7] Z. Guo, S. Zhao, T. Li, D. Su, S. Guo, and G. Wang, 'Recent Advances in Rechargeable Magnesium-Based Batteries for High-Efficiency Energy Storage', *Adv. Energy Mater.*, vol. 10, no. 21, p. 1903591, 2020, doi: 10.1002/aenm.201903591.

[8] D. Aurbach *et al.*, 'Prototype systems for rechargeable magnesium batteries', *Nature*, vol. 407, no. 6805, Art. no. 6805, Oct. 2000, doi: 10.1038/35037553.

[9] M. Deng *et al.*, 'High-energy and durable aqueous magnesium batteries: Recent advances and perspectives', *Energy Storage Mater.*, vol. 43, pp. 238–247, Dec. 2021, doi: 10.1016/j.ensm.2021.09.008.

[10] R. Attias, M. Salama, B. Hirsch, Y. Goffer, and D. Aurbach, 'Anode-Electrolyte Interfaces in Secondary Magnesium Batteries', *Joule*, vol. 3, no. 1, pp. 27–52, Jan. 2019, doi: 10.1016/j.joule.2018.10.028.

[11] R. Mohtadi and F. Mizuno, 'Magnesium batteries: Current state of the art, issues and future perspectives', *Beilstein J. Nanotechnol.*, vol. 5, no. 1, pp. 1291–1311, Aug. 2014, doi: 10.3762/bjnano.5.143.

[12] B. Park and J. L. Schaefer, 'Review—Polymer Electrolytes for Magnesium Batteries: Forging Away from Analogs of Lithium Polymer Electrolytes and Towards the Rechargeable Magnesium Metal Polymer Battery', *J. Electrochem. Soc.*, vol. 167, no. 7, p. 070545, Mar. 2020, doi: 10.1149/1945-7111/ab7c71.

[13] M. Guo, C. Yuan, T. Zhang, and X. Yu, 'Solid-State Electrolytes for Rechargeable Magnesium-Ion Batteries: From Structure to Mechanism', *Small*, vol. 18, no. 43, p. 2106981, 2022, doi: 10.1002/smll.202106981.

[14] H. Shuai, J. Xu, and K. Huang, 'Progress in retrospect of electrolytes for secondary magnesium batteries', *Coord. Chem. Rev.*, vol. 422, p. 213478, Nov. 2020, doi: 10.1016/j.ccr.2020.213478.

[15] P. V. Wright, 'Electrical conductivity in ionic complexes of poly(ethylene oxide)', *Br. Polym. J.*, vol. 7, no. 5, pp. 319–327, 1975, doi: 10.1002/pi.4980070505.

[16] J. Mindemark, M. J. Lacey, T. Bowden, and D. Brandell, 'Beyond PEO—Alternative host materials for Li+-conducting solid polymer electrolytes', *Prog. Polym. Sci.*, vol. 81, pp. 114–143, Jun. 2018, doi: 10.1016/j.progpolymsci.2017.12.004.

[17] C. A. Vincent, 'Ion transport in polymer electrolytes', *Electrochimica Acta*, vol. 40, no. 13, pp. 2035–2040, Oct. 1995, doi: 10.1016/0013-4686(95)00138-5.

[18] S. B. Aziz, T. J. Woo, M. F. Z. Kadir, and H. M. Ahmed, 'A conceptual review on polymer electrolytes and ion transport models', *J. Sci. Adv. Mater. Devices*, vol. 3, no. 1, pp. 1–17, Mar. 2018, doi: 10.1016/j.jsamd.2018.01.002.

[19] S. K. Fullerton-Shirey, L. V. N. R. Ganapatibhotla, W. Shi, and J. K. Maranas, 'Influence of thermal history and humidity on the ionic conductivity of nanoparticle-filled solid polymer electrolytes', *J. Polym. Sci. Part B Polym. Phys.*, vol. 49, no. 21, pp. 1496–1505, 2011, doi: 10.1002/polb.22330.

[20] G. Foran *et al.*, 'The Impact of Absorbed Solvent on the Performance of Solid Polymer Electrolytes for Use in Solid-State Lithium Batteries', *iScience*, vol. 23, no. 10, p. 101597, Oct. 2020, doi: 10.1016/j.isci.2020.101597.

[21] A. Haug, O. Smidsrød, B. Larsen, S. Gronowitz, R. A. Hoffman, and A. Westerdahl, 'The Effect of Divalent Metals on the Properties of Alginate Solutions. II. Comparison of Different Metal Ions.', *Acta Chem. Scand.*, vol. 19, pp. 341–351, 1965, doi: 10.3891/acta.chem.scand.19-0341.

[22] I. Donati, F. Asaro, and S. Paoletti, 'Experimental Evidence of Counterion Affinity in Alginates: The Case of Nongelling Ion Mg2+', *J. Phys. Chem. B*, vol. 113, no. 39, pp. 12877–12886, Oct. 2009, doi: 10.1021/jp902912m.

[23] F. Topuz, A. Henke, W. Richtering, and J. Groll, 'Magnesium ions and alginate do form hydrogels: a rheological study', *Soft Matter*, vol. 8, no. 18, pp. 4877–4881, 2012, doi: 10.1039/C2SM07465F.

[24] K. Y. Lee and D. J. Mooney, 'Alginate: Properties and biomedical applications', *Prog. Polym. Sci.*, vol. 37, no. 1, pp. 106–126, Jan. 2012, doi: 10.1016/j.progpolymsci.2011.06.003.

[25] P. Vadhva *et al.*, 'Electrochemical Impedance Spectroscopy for All-Solid-State Batteries: Theory, Methods and Future Outlook', *ChemElectroChem*, vol. 8, no. 11, pp. 1930–1947, 2021, doi: 10.1002/celc.202100108.

[26] E. von Hauff, 'Impedance Spectroscopy for Emerging Photovoltaics', *J. Phys. Chem. C*, vol. 123, no. 18, pp. 11329–11346, May 2019, doi: 10.1021/acs.jpcc.9b00892.

[27] F. Ciucci, 'Modeling electrochemical impedance spectroscopy', *Curr. Opin. Electrochem.*, vol. 13, pp. 132–139, Feb. 2019, doi: 10.1016/j.coelec.2018.12.003.

[28] V. Abhilash, N. Rajender, and K. Suresh, 'Chapter 14 - X-ray diffraction spectroscopy of polymer nanocomposites', in *Spectroscopy of Polymer Nanocomposites*, S. Thomas, D. Rouxel, and D. Ponnamma, Eds., William Andrew Publishing, 2016, pp. 410–451. doi: 10.1016/B978-0-323-40183-8.00014-8.

[29] Y. Leng, *Materials Characterization: Introduction to Microscopic and Spectroscopic Methods*. John Wiley & Sons, 2009.

[30] P. Gill, T. T. Moghadam, and B. Ranjbar, 'Differential Scanning Calorimetry Techniques:

Applications in Biology and Nanoscience', *J. Biomol. Tech. JBT*, vol. 21, no. 4, pp. 167–193, Dec. 2010.

[31] M. Winter and R. J. Brodd, 'What Are Batteries, Fuel Cells, and Supercapacitors?', *Chem. Rev.*, vol. 104, no. 10, pp. 4245–4270, Oct. 2004, doi: 10.1021/cr020730k.

[32] L. L. Yang, A. R. McGhie, and G. C. Farrington, 'Ionic Conductivity in Complexes of Poly(ethylene oxide) and MgCl2', *J. Electrochem. Soc.*, vol. 133, no. 7, p. 1380, Jul. 1986, doi: 10.1149/1.2108891.

[33] S. Ramalingaiah, D. S. Reddy, M. J. Reddy, E. Laxminarsaiah, and U. V. S. Rao, 'Conductivity and discharge characteristic studies of novel polymer electrolyte based on PEO complexed with Mg(NO3)2 salt', *Mater. Lett.*, vol. 29, no. 4, pp. 285–289, Dec. 1996, doi: 10.1016/S0167-577X(96)00161-9.

[34] K. M. Anilkumar, B. Jinisha, M. Manoj, and S. Jayalekshmi, 'Poly(ethylene oxide) (PEO) – Poly(vinyl pyrrolidone) (PVP) blend polymer based solid electrolyte membranes for developing solid state magnesium ion cells', *Eur. Polym. J.*, vol. 89, pp. 249–262, Apr. 2017, doi: 10.1016/j.eurpolymj.2017.02.004.

[35] C. S. Ramya, S. Selvasekarapandian, T. Savitha, G. Hirankumar, and P. C. Angelo, 'Vibrational and impedance spectroscopic study on PVP–NH4SCN based polymer electrolytes', *Phys. B Condens. Matter*, vol. 393, no. 1, pp. 11–17, Apr. 2007, doi: 10.1016/j.physb.2006.11.021.

[36] J. L. Acosta and E. Morales, 'Synthesis and characterization of polymeric electrolytes for solid state magnesium batteries', *Electrochimica Acta*, vol. 43, no. 7, pp. 791–797, Jan. 1998, doi: 10.1016/S0013-4686(97)00123-0.

[37] A. R. Polu, R. Kumar, K. V. Kumar, and N. K. Jyothi, 'Effect of TiO2 ceramic filler on PEG-based composite polymer electrolytes for magnesium batteries', *AIP Conf. Proc.*, vol. 1512, no. 1, pp. 996–997, Feb. 2013, doi: 10.1063/1.4791378.

[38] M. Ramaswamy, T. Malayandi, S. Subramanian, J. Srinivasalu, and M. Rangaswamy, 'Magnesium ion conducting polyvinyl alcohol–polyvinyl pyrrolidone-based blend polymer electrolyte', *Ionics*, vol. 23, no. 7, pp. 1771–1781, Jul. 2017, doi: 10.1007/s11581-017-2023-z.

[39] R. Manjuladevi, M. Thamilselvan, S. Selvasekarapandian, R. Mangalam, M. Premalatha, and S. Monisha, 'Mg-ion conducting blend polymer electrolyte based on poly(vinyl alcohol)-poly (acrylonitrile) with magnesium perchlorate', *Solid State Ion.*, vol. 308, pp. 90–100, Oct. 2017, doi: 10.1016/j.ssi.2017.06.002.

[40] D. Reber, R. Grissa, M. Becker, R.-S. Kühnel, and C. Battaglia, 'Anion Selection Criteria for Water-in-Salt Electrolytes', *Adv. Energy Mater.*, vol. 11, no. 5, p. 2002913, 2021, doi: 10.1002/aenm.202002913.

[41] M. A. K. L. Dissanayake, L. R. A. K. Bandara, L. H. Karaliyadda, P. A. R. D. Jayathilaka, and R. S. P. Bokalawala, 'Thermal and electrical properties of solid polymer electrolyte PEO9 Mg(ClO4)2 incorporating nano-porous Al2O3 filler', *Solid State Ion.*, vol. 177, no. 3, pp. 343–346, Jan. 2006, doi: 10.1016/j.ssi.2005.10.031.

[42] E. Bortel, S. Hodorowicz, and R. Lamot, 'Relation between crystallinity degree and stability in solid state of high molecular weight poly(ethylene oxide)s', *Makromol. Chem.*, vol. 180, no. 10, pp. 2491–2498, 1979, doi: 10.1002/macp.1979.021801023.

[43] R. Deivanayagam *et al.*, 'Composite Polymer Electrolyte for Highly Cyclable Room-

Temperature Solid-State Magnesium Batteries', *ACS Appl. Energy Mater.*, vol. 2, no. 11, pp. 7980–7990, Nov. 2019, doi: 10.1021/acsaem.9b01455.

Appendix

Synthesis parameters of the solid polymer electrolyte

Composition	Amount of PEO (g)	Amount of Mg-alginate (g)	Amount of $MgCl_2 \cdot 6H_2O$ (g)	Water (ml)
PEO90Alginate10	0.45	0.05	0.1	1.5
PEO80Alginate20	0.4	0.1		1.75
PEO70Alginate30	0.35	0.15		1.75
PEO60Alginate40	0.3	0.2		2

Another result of study on the variation of the alginate content in PEO – Mg-alginate – $MgCl_2 \cdot 6H_2O$ system

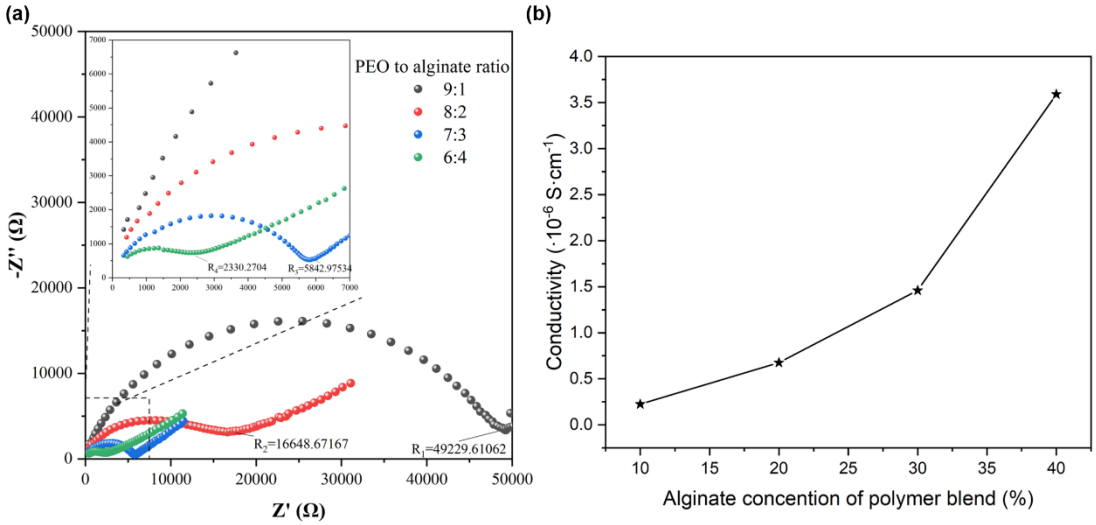

Another result of galvanostatic cycling

This graph also exhibits the neck phenomenon in the discharge voltage profile around 100 cycles. The difference in the charging and discharging voltage profiles is probably due to the difference of the two Mg electrodes. The surfaces may not be the same degree of evenness.

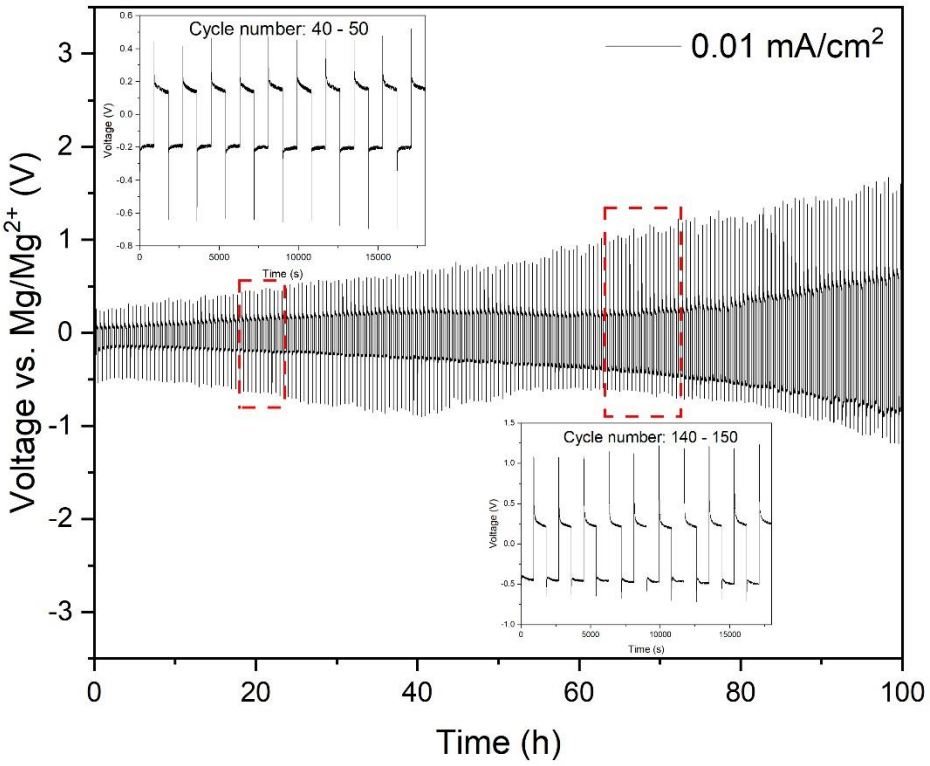
0.01 mA/cm2
Cycle number: 40 - 50
Cycle number: 140 - 150
Voltage (V)
Time (s)
Voltage vs. Mg/Mg2+ (V)
Time (h)